

Report on  
Plans of the Beams Division  
for  
TeV33

January 29, 1997

J. Marriner, editor

Contributors:

P. Bagley  
F. Bieniosek  
M. Church  
J. Johnstone  
I. Kourbanis  
D. McGinnis  
S. Ngaitsev  
R. Pasquinelli  
S. Shukla  
S. Werkema

<b>1. COLLIDING BEAM PARAMETERS &amp; OVERVIEW</b>	<b>4</b>
1.1 Collider Luminosity	5
1.2 Importance of Antiproton Production	6
1.3 Importance of Beam-Beam Effect	7
1.4 Tev33 overview and parameters	8
<b>2. ASSUMED CONDITIONS</b>	<b>9</b>
2.1 Main Injector	9
2.2 Recycler	10
2.3 Tevatron Energy	10
2.4 Proton Removal	10
<b>3. ANTIPROTON PRODUCTION</b>	<b>11</b>
3.1 Proton Intensity at the Antiproton Target	12
3.1.1 Linac & Booster performance	13
3.1.2 Main Injector performance	14
3.1.3 Slip stacking	15
3.2 Antiproton Target	22
3.2.1 Beam sweeping	22
3.2.2 Lithium lens mechanical issues	24
3.2.3 Radiation damage issues	24
3.2.4 Antiproton target radiation shielding and environmental issues	25
3.2.5 Conclusion	25
3.3 Antiproton Acceptance	25
3.3.1 Lithium Lens Gradient	25
3.3.2 Transverse aperture increase to $32\pi \times 32\pi$	26
3.3.3 Momentum aperture increase	30
3.4 Antiproton Bunch Rotation	31
3.5 Antiproton Cooling Overview	32
3.6 Transverse Cooling in the Debuncher	34
3.7 Debuncher Momentum Cooling	36
3.8 Longitudinal Stacking in the Accumulator	38
3.9 Stochastic Cooling Technology	41

3.9.1 4-8 Ghz Pickups	41
3.9.2 4-8 GHz Signal Transmission	43
<b>3.10 Antiproton Electron Cooling</b>	<b>45</b>
3.10.1 Electron Cooling Rate	45
3.10.2 Electron Beam Optics	46
3.10.3 Technical Considerations	47
3.10.4 Alternative approaches	49
<b>4. COLLIDING BEAMS ISSUES</b>	<b>49</b>
4.1 Tevatron Injection	49
4.2 Proton Intensity	50
4.3 Antiproton Intensity	52
4.4 Tevatron rf voltage considerations	52
4.5 Single beam stability	55
4.6 Beam abort	56
4.7 Interaction Regions	57
4.8 Beam-beam effects	63
4.8.1 Tune footprint	65
4.8.2 Crossing angle	65
4.9 Luminosity Leveling	65
<b>5. SUMMARY OF UPGRADES REQUIRED.</b>	<b>66</b>
<b>6. RISKS &amp; ALTERNATIVE APPROACHES</b>	<b>68</b>
6.1 Strip-line kicker	68
6.2 Full MI targeting	68
6.3 Risks	68
<b>7. CONCLUSION</b>	<b>68</b>

## 1. Colliding beam parameters & Overview

The Tevatron antiproton collider achieved peak a luminosity of  $2.5 \times 10^{31} \text{ cm}^{-2} \text{ sec}^{-1}$  in Run I, which ended in February 1996. The Main Injector and associated upgrades are expected to enable luminosities in the range of  $5\text{-}8 \times 10^{32} \text{ cm}^{-2} \text{ sec}^{-1}$  in Run II, which is scheduled to begin in

1999. The Main Injector and the associated colliding beams upgrades are sometimes collectively referred to as Fermilab III. The addition of the Recycler Ring to the Main Injector project is expected to improve the antiproton utilization efficiency and increase the luminosity by a factor of 2 to 3.

The goal of the TeV33 project is to increase the peak luminosity to the vicinity of  $10^{33}$   $\text{cm}^{-2}\text{sec}^{-1}$ . A more specific goal of obtaining  $30 \text{ fb}^{-1}$  by the year 2006 was suggested in the TeV2000 committee report.<sup>1</sup> The TeV33 period of collider running is also referred to as Run III.

Table I is the working parameter table for Run II. It illustrates the changes required to achieve the Run II luminosity goals and also the benefits of antiproton recycling. Run II requires a modest improvement in proton intensity and about 8 times more antiprotons (spread over 6 times more bunches). The antiproton stacking rate is required to increase substantially (about a factor of 3) to produce the necessary antiprotons. The Run II luminosity also benefits from the smaller (2 eV-sec) longitudinal emittances expected from the Main Injector, the higher energy (1000 GeV instead of 900 GeV) Tevatron, and the higher antiproton transmission efficiency of the Main Injector.

Table I. Working parameter table for Run II.

Parameter	Run IB (1993-95)*	Run II (w/Recycler)	Units
Protons/bunch	$23 \times 10^{10}$	$27 \times 10^{10}$	
Antiprotons/bunch	$5.5 \times 10^{10}$	$7.5 \times 10^{10}$	
Req'd Pbar Production Rate	6	20	$10^{10}/\text{hr}$
Proton emittance (95%, norm)	$23\pi$	$20\pi$	mm-mrad
Antiproton emittance (95%, norm)	$13\pi$	$15\pi$	mm-mrad
Energy	900	1000	GeV
No. of Bunches	6	36	
Bunch length (rms)	0.60	0.38	m
Form Factor	0.59	0.73	
Typical Luminosity	$1.6 \times 10^{31}$	$2.1 \times 10^{32}$	$\text{cm}^{-2} \text{sec}^{-1}$
Bunch Spacing	~3500	396	nsec
Interactions per crossing	2.7	5.8	

\*Run IB column represents average of 32 stores over the period March 8-April 21, 1995.

### 1.1 Collider Luminosity

The luminosity of the Tevatron collider may be written as

$$\mathcal{L} = \frac{3\gamma f_0}{\beta^*} (BN_{\bar{p}}) \left( \frac{N_p}{\epsilon_p} \right) \frac{F(\beta^*, \theta_x, \theta_y, \epsilon_p, \epsilon_{\bar{p}}, \sigma_z)}{(1 + \epsilon_{\bar{p}}/\epsilon_p)}$$

[1]

where  $\gamma_r = E/mc^2$  is the relativistic energy factor,  $f_0$  is the revolution frequency, and  $\beta^*$  is the beta function at  $s=0$  (where it is assumed to attain the same minimum in each plane). The proton (antiproton) beam transverse emittance  $\epsilon_p(\epsilon_{\bar{p}})$  is defined to be  $\epsilon = 6\pi\gamma_r\sigma^2/\beta$  for a bunch with a

gaussian distribution and assumed to be the same in both transverse planes,  $B$  is the number of bunches,  $N_p$  ( $N_{\bar{p}}$ ) is the number of protons (antiprotons) per bunch,  $\theta_x$  and  $\theta_y$  are the crossing half-angles,  $\sigma_z$  is the derived from the rms proton and antiproton bunch lengths  $\sigma_z^2 = (\sigma_{zp}^2 + \sigma_{z\bar{p}}^2)/2$  and  $F \leq 1$  is a form-factor that accounts for the depth of focus (hour glass) and crossing angle effects on the luminosity caused by non-zero bunch lengths. The bunch lengths depend on the longitudinal emittance and the rf voltage, but the luminosity depends only on the bunch lengths. In Run II, the form-factor is dominated by the hour-glass effect (the design crossing-angle is 0). For gaussian beams the hour-glass effect may be written as:

$$F = \frac{\sqrt{\pi}\beta}{\sigma_z} e^{\frac{\beta^2}{\sigma_z^2}} \operatorname{erfc}\left[\frac{\beta}{\sigma_z}\right] \quad [2]$$

where  $\sigma_z^2 = (\sigma_{zp}^2 + \sigma_{z\bar{p}}^2)/2$  and the complementary error function is related to the error function by  $\operatorname{erfc}(z) = 1 - \operatorname{erf}(z)$ . For TeV33 the crossing angle effect is large and the luminosity comes mainly from the  $z=0$  region where the hour glass effect is small. In this case the form-factor  $F$  may be written as

$$F = \frac{1}{\sqrt{1 + \sigma_z^2(\theta_x^2/\sigma_x^2 + \theta_y^2/\sigma_y^2)}} \quad [3]$$

where  $\sigma_x^2 = (\sigma_{xp}^2 + \sigma_{x\bar{p}}^2)/2$  and similarly for  $y$ .

The luminosity formula ([1]) is written to emphasize the major issues in achieving high luminosity. The first quantity in parenthesis is the total number of antiprotons. Under current and probably future operating conditions, the most important factor contributing to the achievable luminosity is the total number of antiprotons in the ring,  $BN_{\bar{p}}$ . The second most important factor is the proton phase space density,  $N_p/\varepsilon_p$ , which is constrained by the need to limit the beam-beam tune shift. The form-factor ( $F$ ) and the emittance ratio factor  $\varepsilon_p/(\varepsilon_p + \varepsilon_{\bar{p}})$  are important, but they can not exceed unity and the amount of luminosity that can be gained using these factors is limited.

## 1.2 Importance of Antiproton Production

Of the many technical issues involved with high luminosity proton-antiproton colliders, there is probably no more fundamental limitation than requirement that antiprotons must be produced at a higher rate than the rate at which they are consumed in collisions.

The Run II luminosity is expected to increase to  $2 \times 10^{32} \text{ cm}^{-2}\text{sec}^{-1}$  from the Run I value of  $2 \times 10^{31} \text{ cm}^{-2}\text{sec}^{-1}$ . Much of the gain comes from a more efficient consumption of antiprotons. In particular, it is expected that the Main Injector will improve the antiproton transmission and coalescing efficiency and that the Recycler will make possible the recovery ("recycling") of antiprotons at the conclusion of a Tevatron store.

It is easy to calculate the minimum antiproton production rate required to support a given luminosity by calculating the loss rate from beam-beam collisions. This loss rate is:

$$\Phi_{\bar{p}}^{(\min)} = n_c \sigma_a \mathcal{L} \quad [4]$$

where  $n_c$  is the number of collision points and  $L$  is the luminosity. The cross-section is the cross-section for scattering outside the acceptance of the Tevatron. This cross-section is only slightly less than the total cross-section. We assume that  $\sigma_a$  is 70 mb at 1000 GeV. With 2 collision points at a peak luminosity of  $10^{33} \text{ cm}^{-2}\text{-sec}^{-1}$  a minimum antiproton production rate of  $1.4 \times 10^8 \text{ sec}^{-1}$  is required. The actual production rate requirement includes all the other antiproton loss mechanisms (not just loss through collisions). We define the antiproton utilization efficiency to be the number of antiprotons consumed in high energy collisions divided by the number of antiprotons produced. It follows that the average luminosity is determined by the product of antiproton production rate and the utilization efficiency. The Run Ib antiproton utilization efficiency, based on a 10 week period where  $32 \text{ pb}^{-1}$  was accumulated was about 8%.\* The larger apertures in the Main Injector (compared to the Main Ring), higher efficiency in coalescing antiprotons, and the recycling of antiprotons should substantially increase this efficiency. We assume that this efficiency will reach 50% in Run II and be maintained thereafter.

The average luminosity is much less than the peak luminosity. Based on operational experience, the average luminosity is about 1/3 the peak luminosity, and the required antiproton flux is therefore about 1/3 that calculated above. The difference in peak and average luminosity occurs because there are times when colliding beams are not present (about 1/3 of the time) and because the luminosity decays during the course of a store. However, the average stacking rate is reduced by similar factors: stacking occurs about 60-70% of the hours scheduled for operation and the average stacking rate is about 1/2 of the best stacking rates. The average stacking rate is reduced from the peak values because of equipment malfunctions, drifts in operating conditions that can not be or are not properly compensated, and the decrease in stacking rate that occurs at large stacks. The latter factor should be alleviated in Run II, when the Accumulator will transfer its antiproton stack to the Accumulator after a few hours of stacking. Thus, we estimate that both the average luminosity and average stacking rate are equal to about 1/3 their peak values.

We conclude that peak stacking rates of about  $10^{12}$  antiprotons per hour are required to support two interaction regions at  $10^{33} \text{ cm}^{-2}\text{-sec}^{-1}$ . This rate is a 10-fold increase in stacking rate over the Tevatron I design, a 14-fold increase over the best stacking rate achieved, and a 5-fold increase over the projected Run II stacking rate. Clearly, dramatic increases in the antiproton production rate are an essential element of any plan to achieve a luminosity of  $10^{33} \text{ cm}^{-2}\text{-sec}^{-1}$  in the Tevatron proton-antiproton collider.

### 1.3 Importance of Beam-Beam Effect

The formula for the (linear) antiproton beam-beam tune shift with no crossing angle is:

$$\begin{aligned} \Delta\nu &= 6 \frac{r_p}{4\pi} n_c \frac{N_p}{\epsilon_p} \\ &= 0.0073 (\pi \text{ mm} - \text{mrad}/10^{10}) n_c \frac{N_p}{\epsilon_p} \end{aligned} \quad [5]$$

where  $r_p$  is the classical proton radius ( $1.535 \times 10^{-18} \text{ m}$ ) and  $n_c$  is the number of interaction points. Operating experience in the Tevatron suggests that the maximum tolerable beam-beam tune shift lies in the range 0.02 to 0.025.

When the beam-beam tune shift is caused primarily by head-on interactions at zero crossing-angle, the beam-beam tune shift determines the maximum value of the factor  $N_p/\epsilon_p$ ,

---

\* In those 10 weeks  $5.7 \times 10^{13}$  antiprotons were accumulated and  $32 \text{ pb}^{-1}$  were delivered to each of the two experiments.

which appears in Eqn. [1]. For TeV33, the formula (Eqn. [5]) does not apply. In TeV33, the beams cross at an angle to avoid unwanted beam-beam interactions near the interaction region. The crossing angle at the interaction region dramatically reduces the beam-beam tune shift (some higher order effects increase), and the sum of the long range interactions cause tune shifts comparable to those at the interaction points. These crossing angle and long range effects depend on both  $N_p$  and  $\epsilon_p$  separately, and, may partially cancel depending on the detailed geometry of the beams and their orbits. These issues are discussed in considerably more detail in section 4.8. Despite the complicated nature of the beam-beam interaction, the proton beam parameters for TeV33 are consistent with a naive application of Eqn. [5].

#### **1.4 Tev33 overview and parameters**

The general strategy to increase the Tevatron proton-antiproton collider is to produce antiprotons at a much higher rate and to maintain the Run II antiproton utilization efficiency. This goal can be accomplished if the antiproton production rate can be increased and the emittances held at their Run II values. Some possible TeV33 parameters are given in Table II. The antiprotons are distributed into more bunches (90 for TeV33 versus 36 for Run II). The number of bunches is determined primarily by the desire of the experiments to keep the number of interactions per beam crossing as low as possible. However, at least for the parameters shown in Table II, the number of bunches would have to increase to avoid excessive proton beam tune shifts (caused by high intensity antiproton bunches). The TeV33 parameters are, at this point, still speculative. It is quite possible that we will choose to obtain higher luminosity by making the bunches smaller in some dimension. One version (with improved rf focusing) is shown in Table II. For the parameters given the bunch length is reduced from 35 cm to 15 cm and the form-factor is increased from 0.52 to 0.79. Other factors appearing in the luminosity formula can also be manipulated by various techniques. However, the *integrated* luminosity can be increased by at most a factor of 2 over the assumed antiproton utilization efficiency of 50%, because the integrated luminosity is limited by the production rate of antiprotons.



**Table II. Possible TeV33 Parameter Tables**

Parameter	No Upgrades	rf upgrade	Units
Protons/bunch	$27 \times 10^{10}$	$27 \times 10^{10}$	
Antiprotons/bunch*	$27 \times 10^{10}$	$27 \times 10^{10}$	
Proton emittance (95%, norm)	$20 \pi$	$20 \pi$	mm-mrad
Antiproton emittance (95%, norm)	$20 \pi$	$20 \pi$	mm-mrad
Beam Energy	1000	1000	GeV
No. of Bunches	90	90	
Longitudinal Emittance	2	2	eV-sec
rf Frequency	53	212	MHz
rf Voltage	1	16	MV
Bunch length (rms)	0.36	0.13	m
Crossing Half-angle	0.17	0.17	mrاد
Form Factor	0.36	0.72	
Typical Luminosity	$0.8 \times 10^{33}$	$1.7 \times 10^{33}$	$\text{cm}^{-2}\text{sec}^{-1}$
Number of IR's	2	2	
Bunch Spacing	132	132	nsec
Interactions per crossing	7.8	15.6	

\*The maximum antiproton intensity is assumed to be equal to the proton intensity for the purposes of the luminosity calculation. Actual antiproton intensities will fluctuate from store to store.

## 2. Assumed conditions

### 2.1 Main Injector

The Main Injector is a project that will result in the replacement of the Main Ring by a smaller, larger aperture ring known as the Main Injector. The Main Injector project is nearing completion and is described in detail in the Main Injector Design Handbook.<sup>2</sup> Some of the major goals of the Main Injector project, relevant to TeV33 are listed in Table III. This document assumes that all of these goals will be met.

**Table III. Main Injector Project Goals**

Parameter	Goal	
Intensity per bunch	$6 \times 10^{10}$	
Total Pbar production intensity	$5 \times 10^{12}$	(84 bunches)
Proton beam transverse emittance	$12\pi$	mm-mrad
Proton beam longitudinal emittance	0.2	eV-sec
Main Injector transverse admittance (@8.9 GeV)	$40\pi$	mm-mrad
Main Injector longitudinal admittance (@8.9 GeV)	0.5	eV-sec
Coalesced bunch intensity	$3e^{11}$	(per bunch)
Coalesced bunch transverse emittance	$12\pi$	mm-mrad
Coalesced bunch longitudinal emittance	2.0	eV-sec

## 2.2 Recycler

The Recycler is described elsewhere.<sup>3</sup> The most important design goal is to recover, on average, 50% of the antiprotons that could potentially be recovered. This goal could be met, for example, if 75% of the antiprotons are recovered from the 75% of the stores that end normally<sup>†</sup>. We assume that we will continue to achieve the 50% antiproton recovery efficiency for TeV33 despite the increased number of bunches, the higher intensities, and (possibly) somewhat larger emittances.

## 2.3 Tevatron Energy

We have specified that the Tevatron will run at 1000 GeV in Run II and future runs. We have finished an upgrade to the cryogenic cooling system and have accelerated protons to 980 GeV. The plan to achieve 1000 GeV operation involves running some satellite refrigerators at lower pressure (and therefore a lower temperature) and some shuffling of magnets. It is clear that the ultimate energy limit of the Tevatron lies near 1000 GeV, but it is not clear whether we will be able to run reliably at 1000 GeV. The precise operating energy will depend on our success at optimizing the operation of the cryogenic systems (including possible improvements) and at mitigating the problem of low quench-current magnets.

## 2.4 Proton Removal

In order to recycle the antiprotons, they must be separated from the protons. We plan to eliminate the protons at the end of a Tevatron store, before deceleration. This plan has the advantage of making the deceleration process much easier because of the absence of beam-beam interaction effects. However, it does require removal of the protons from the Tevatron at high field, when the Tevatron magnets have the least margin against quenches induced by beam loss. While we have substantial experience with removing the protons with scrapers for special experiments (the proton and antiproton beams are spatially separated), it typically takes half an hour to complete the process. Improvements both in technique and speed would be highly desirable. At the moment, it is uncertain how this goal will be accomplished in Run II.

The Tev33 parameters require the removal of about 3 times the number of proton bunches. The techniques established for Run II may require modification. We assume that an adequate solution will be found based on Run II experience.

<sup>†</sup> In Run Ib 71% of the stores were intentionally terminated. The others typically ended because of the failure of some critical component.

### 3. Antiproton Production

The strategies for increasing the antiproton production fall into three categories:

- 1) Increase the number of protons targeted per pulse
- 2) Increase the proton beam pulse rate
- 3) Increase the antiproton collection efficiency

Relative to the Run II parameters, we plan to increase the number of protons targeted (by a factor of 1.9), to decrease the pulse rate by 25%, and to increase the antiproton collection efficiency (by a factor of 3.4), for a net increase in the antiproton flux of 4.8. The decrease in repetition rate is largely to allow more time per cycle for stochastic cooling although some decrease is required to accommodate the increased number of Booster cycles for slip stacking (see 3.1.3)

Table IV shows the numerology of antiproton production during Collider Run 1b and the production that would be expected in Collider Run II in the absence of upgrades to the target station, the injection line (AP-2), and the Debuncher apertures (assuming also that only a single Booster batch is targeted). The gain in production is due to the increased proton intensity on target and the increased repetition rate. Without the target sweeping system (described below), the yield (antiprotons produced per proton) would decrease because the proton beam spot size would need to be increased in order to keep the deposited energy density in the nickel target below 800 J/g. Assuming perfect Debuncher to Accumulator transfer efficiency, the maximum stacking rate in Run II will be  $21.4 \times 10^{10}$ /hour. In Run 1b, the Debuncher to Accumulator transfer efficiency was 80%, and the Accumulator stacking efficiency (rf stacking plus stacktail momentum cooling) was 90%. Upgrades to the Debuncher and Accumulator stochastic cooling systems are expected to increase these two efficiencies for Run II.

Table IV. Comparison of Run Ib and Run II antiproton source upgrades.

	Run 1b	Run II no upgrades
protons/pulse on target ( $10^{12}$ )	3.2	5.0
cycle time (sec)	2.4	1.5
yield into Deb. ( $\bar{p}$ / $10^6$ proton)	21.0	17.8
$\bar{p}$ /pulse into Deb. ( $10^7$ )	6.7	8.9
$\bar{p}$ /hour into Deb. ( $10^{10}$ )	10.1	21.4
initial Deb. emit. ( $\pi$ -mm-mrad)	16.0	16.0

There are several upgrades which greatly increase the antiproton flux into the Debuncher in Run II and beyond:

- 1) Beam sweeping: By sweeping the proton beam in a small circle on the target during the 1.6  $\mu$ sec spill, the energy deposition can be spread out over a larger volume of the target, and therefore the beam spot size can be made smaller, which increases the yield. The antiproton beam downstream of the target is then swept to remove the circular motion. In the absence of beam sweeping, each factor of 2 increase in

proton intensity on target requires that the beam spot size be enlarged causing the antiproton yield to drop by 15-20%.

- 2) AP-2/Debuncher transverse aperture increase: The measured transverse emittance of beam entering the Debuncher is  $15\pi \times 16\pi$ , and the measured acceptance of the Debuncher is  $29\pi \times 26\pi$ . Increasing the AP-2/Debuncher transverse aperture to  $32\pi \times 32\pi$  will increase the yield into the Debuncher by a factor of 2.6.
- 3) Lithium lens improvements: Currently the lens operates at 750 T/m. Modest improvements to the original design may permit reliable operation at 900 T/m, which will increase the yield by 17% under current conditions.
- 4) Development of new lens design involving liquid lithium could allow reliable operation at 1200 T/m, with a further increase in yield. We are still investigating the feasibility of the lithium lens.
- 5) Momentum aperture increase: The full momentum acceptance of the Debuncher is currently measured to be 4%. By ramping the slip factor  $\eta$  to .003 at injection, the momentum aperture can be increased by 18%, which increases the yield by 18%.

In addition to the above improvements, "slip stacking" in the Main Injector (longitudinally stacking more than one Booster batch of protons into the MI in each 120 GeV beam cycle) may increase the integrated number of protons on target by a factor of 1.9 (see section 3.1.3). Table V summarizes the possible gains that can be made in antiproton production and collection with the above upgrades. The table lists the cumulative gains in yield and production. The order is arbitrary; the factors that increase the antiproton flux are largely independent. We note that many of these

Table V. Summary of antiproton yield and production improvements for TeV33

Upgrade	Factor	Yield into Deb. ( $\bar{p}$ / $10^6$ proton)	( $\bar{p}$ /hour into Deb. ( $10^{10}$ ))
Run II (without upgrades)	1.00	17.8	21.4
Beam sweeping	1.18	21.0	25.3
Slip stacking	1.90	21.0	48.1
$32\pi \times 32\pi$	2.59	54.4	65.4
Debuncher $\Delta p/p$ increase	1.18	64.2	124.5
Lithium lens to 900 T/m	1.11	71.3	138.2
Repetition Rate	0.75	71.3	103.6
Liquid lithium lens	1.09	77.7	113.0

While there are a number of techniques available to increase the antiproton flux, there is no realistic alternative to improved antiproton cooling. The plan for TeV33 requires higher frequency stochastic cooling in the 4-8 Ghz band and the introduction of electron cooling in the Recycler. The cooling is discussed in section 3.5.

### 3.1 Proton Intensity at the Antiproton Target

Increasing the intensity of the proton beam at the antiproton target is one technique to increase the antiproton flux. The higher intensity proton beam is difficult to accommodate in the target station because of the high peak energy deposition in the target, possible radiation damage to

the target station components, and the need to shield personnel and the environment from excessive radiation. The TeV33 plan calls for an increase in proton intensity by a factor of 1.9 through the slip stacking technique described in section 3.1.3.

### 3.1.1 Linac & Booster performance

Run II specifications call for the Booster to produce  $5 \times 10^{12}$  protons per pulse with a maximum transverse emittance of  $20\pi$  mm-mrad. The maximum Booster intensity achieved to date is  $4.4 \times 10^{12}$ , but the Booster normally operates at lower intensity in order to achieve the smaller emittance required by the Main Ring, where the effective normalized acceptance is about  $13\pi$  mm-mrad. The Booster is expected to reach its goal of  $5 \times 10^{12}$  after a period of operation with the Main Injector.

Improvements in Booster intensity beyond those already expected would be useful in producing lower emittance proton beams in collisions and for producing antiprotons at a higher rate. The Linac intensity is probably not of primary importance because beam can be injected for multiple turns using  $H^-$  ions. Most proposals for increased Booster performance involve fairly expensive Linac energy upgrades or construction of a larger aperture Booster to overcome space-charge effects. The more modest plans to improve the Booster aperture for Run II may be more effective than now anticipated. For the moment, it seems prudent not to rely on anything but incremental improvements in Booster intensity.

We now plan that the Booster longitudinal emittance will to be 0.1-0.2 eV-sec for Main Injector operation, but the Booster appears to be capable of producing beams<sup>4</sup> of 0.07 eV-sec. Figure 1 shows the measured longitudinal emittance versus intensity in the Booster. The solid curve, represents measurements taken with the old, 200-MeV Linac; the dashed curve was taken after the upgrade to 400 MeV. The improvement in longitudinal emittance is not the direct result of the 400 MeV upgrade, but the result of suppressing a longitudinal coupled bunch instability.

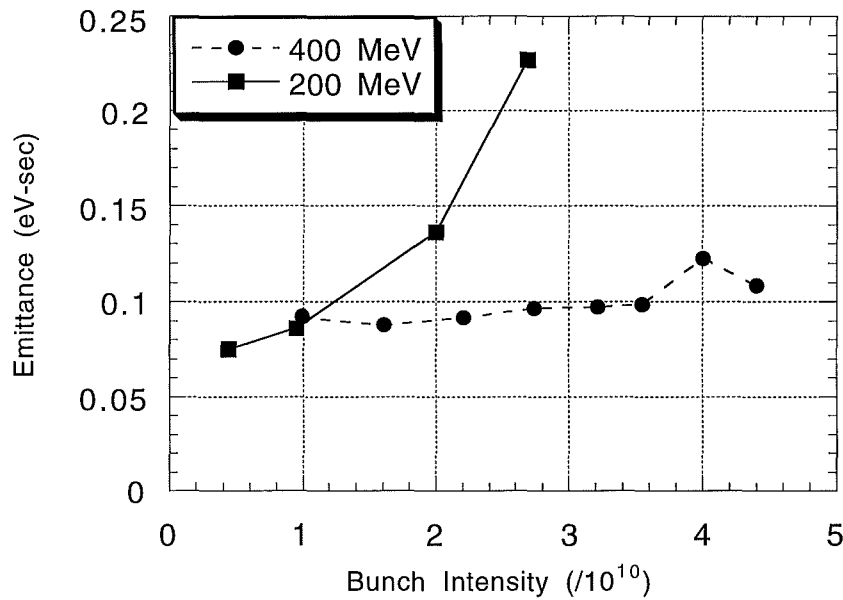


Figure 1. The Booster longitudinal emittance before and after the Linac upgrade.

### 3.1.2 Main Injector performance

The Main Injector was designed, in part, to accept the large emittance beams that one might expect on the basis of the extrapolation of the solid curve in Figure 1. We are left with the rather pleasant situation that the momentum spread of the Booster beam is considerably smaller than the momentum acceptance of the Main Injector. We may be able to take advantage of the unexpected improvement in beam emittance by stacking multiple pulses into the Main Injector.

The ultimate Main Injector intensity limitation is not known either experimentally or theoretically. However, compared to the Main Ring, the Main Injector has a much larger aperture and more attention has been paid to achieving a low beam impedance. These features are expected to result in substantially higher beam currents. One known limitation is the amount of rf power available: the Main Injector can support  $10^{11}$  particles per bunch without modification (the nominal design intensity is  $6 \times 10^{10}$ ).

The Laslett tune shift for the Main Injector (space charge plus image charge) has been calculated (see reference 2) to be -0.08 for  $6 \times 10^{10}$  protons per bunch, but the maximum tolerable tune shift is unknown. The tune shift limit could possibly be increased with a improved resonance compensation scheme in the Main Injector or the transverse or longitudinal emittances could be increased to decrease the tune shift. The increased emittances would have an effect on antiproton production (the effect of the longitudinal emittance on bunch rotation is discussed in section 3.4), but the emittance effects are weaker than the intensity effect.

Other collective effects such as unstable beam motion could make it difficult for the Main Injector to operate at higher per bunch intensities. We have extensive experience damping instabilities in the Main Ring and we should be able to damp dipole instabilities. Other instabilities, such as microwave type instabilities, could be more difficult to handle.

### 3.1.3 Slip stacking

The most promising strategy to increase the beam intensity seems to be to stack Booster pulses in the Main Injector. The most promising technique appears to be to coalesce bunches in the Main Injector with a technique known as "slip stacking". Slip stacking is particularly attractive because it requires no major hardware and could be implemented at the *beginning* of Run II. A cartoon of the stacking process is shown in Figure 2. A similar technique has been used at the CERN Proton Synchrotron (PS).<sup>5</sup>

According to the current plan for Run II, the 120 GeV protons used in antiproton production will be obtained by transferring one Booster batch into the Main Injector at 8 GeV and accelerating it to 120 GeV. The proton intensity can be nearly doubled using 'slip stacking' in the Main Injector. This involves stacking two Booster batches end to end, but with slightly differing momenta, into the Main Injector. The two batches have different periods of revolution and 'slip' relative to each other azimuthally and finally overlap. When they overlap they are captured using a single rf which is the average of the initial frequencies associated with the two batches. Since the Booster and Main Injector acceleration cycles are 66 ms and 1.5s respectively, the need for an extra Booster cycle increases the total antiproton production cycle by less than 0.1 sec and is a small effect on the total cycle time. We have planned for the TeV33 production cycle to be 2.0 sec. This cycle time is long enough to load the Main Injector with 6 Booster batches, slip stack one batch (to be used for pbar production) and to extract the other 5 batches for fixed target experiments. Slip stacking on all 6 batches (12 Booster cycles) is, in principle, possible, but requires a longer Main Injector cycle.

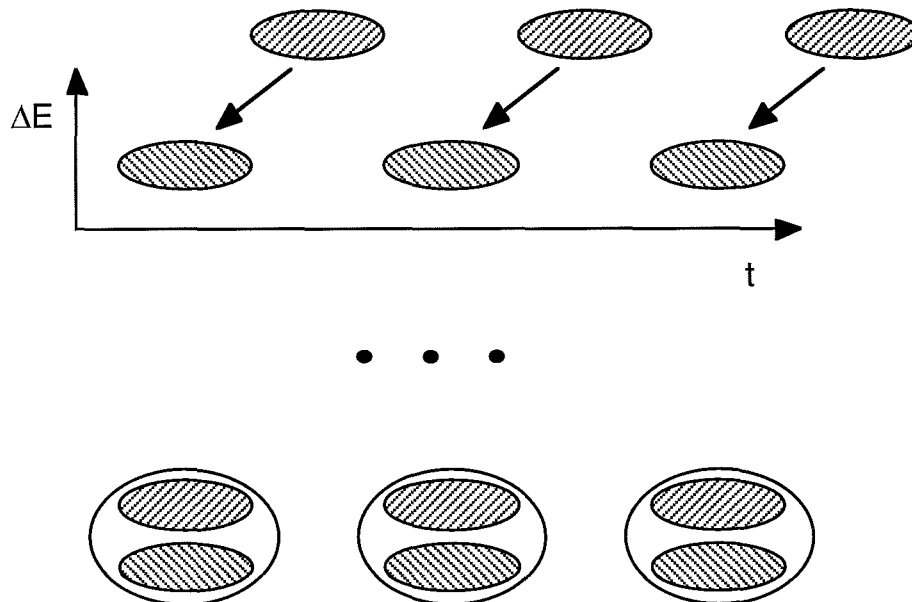


Figure 2. A cartoon of slip stacking. Two batches of beam are displaced in azimuth and energy (above), are brought close to each other, and are then combined in a single, large bucket.

The following is a list of factors that determine the optimum momentum separation between the two batches, initially and before they are coalesced, and the rf voltages involved.

- 1) A larger momentum separation reduces the time before the batches can be coalesced.
- 2) A larger momentum separation requires a larger horizontal aperture.
- 3) A smaller momentum separation just before the batches are coalesced leads to a smaller longitudinal emittance for the final beam, if the effect of the second rf system is small.
- 4) The rf buckets for the two batches get more distorted as the separatrices move closer together. The losses become fairly high if the separatrices overlap. So the beams should spend as little time with their separatrices close together as possible before they are coalesced.

The procedure used to find a way to obtain a final coalesced beam of small emittance containing a reasonably large fraction of the initial beams, consists of two steps. The first step, described in more detail in section 3.1.3.1, consists of finding the approximate heights of the initial buckets and that of the final bucket after coalescing, which would result in a final beam of small longitudinal emittance with small losses during coalescing. We ignore the distortion of the rf buckets due to multiple frequencies in this step. In the next step, which is described in section 3.1.3.2, we use these approximate heights of the buckets as starting points and use rf simulations that include the distortion of the buckets, to find an acceptable strategy of rf manipulations to achieve our goals and to estimate the final emittance of the beam and the losses during coalescing when we use the strategy.

In Section 3.1.3.3 we estimate the effects of beam loading and consider ways to overcome its adverse effects. The effects are serious due to the high intensity of the proton beam. Compensating for the effects is complicated by the simultaneous presence of two beams and rf systems.

### 3.1.3.1 Optimum rf bucket heights

The optimum bucket heights before and after coalescing were found assuming gaussian particle distributions for the initial beams. The harmonic number is 588 and rf frequency is approximately 53 MHz respectively. We assume a 0.15 eV-s longitudinal emittance for each of the initial beams. This value is the measured emittance in the Main Ring at injection. The emittance in the Main Injector is expected to be lower due to improved Booster performance. The height of a bucket with area 0.15 eV-s is 6.15 MeV.

For given heights of the initial and final buckets after coalescing, the area of the beam contour in the final bucket containing 95% of the initial beam was found by integrating the part of the initial gaussian distribution within the contour. The process was repeated for various heights of the final bucket. Figure 3 shows the area corresponding to various final bucket heights, for an initial bucket height of 6.2 MeV. The height that gave the minimum area was chosen as optimum final bucket height for the given initial bucket. The process was repeated for various values of the initial bucket height. Figure 4 shows the optimum final bucket heights and the heights of the corresponding beam contours containing 95% of the beam for various initial bucket heights. Figure 5 shows the minimum area containing 95% of the beam for various initial bucket heights.



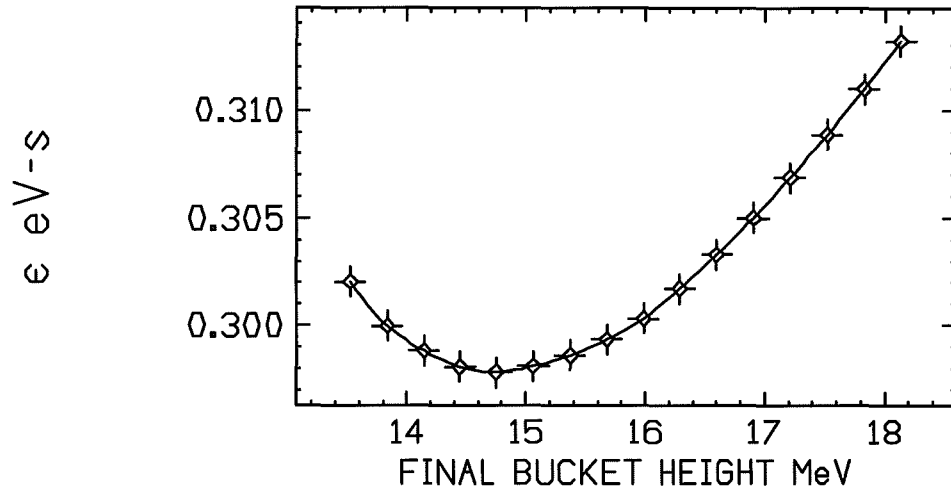


Figure 3. Area containing 95% of beam vs final bucket height for an initial bucket height of 6.2 MeV.

Even if the injected beams are gaussian, the beam distributions before coalescing are not expected to be gaussian if the two rf systems have frequencies that are close together. The distortion of the distributions due to the presence of the second rf was determined using a tracking simulation and is described in section 3.1.3.2.

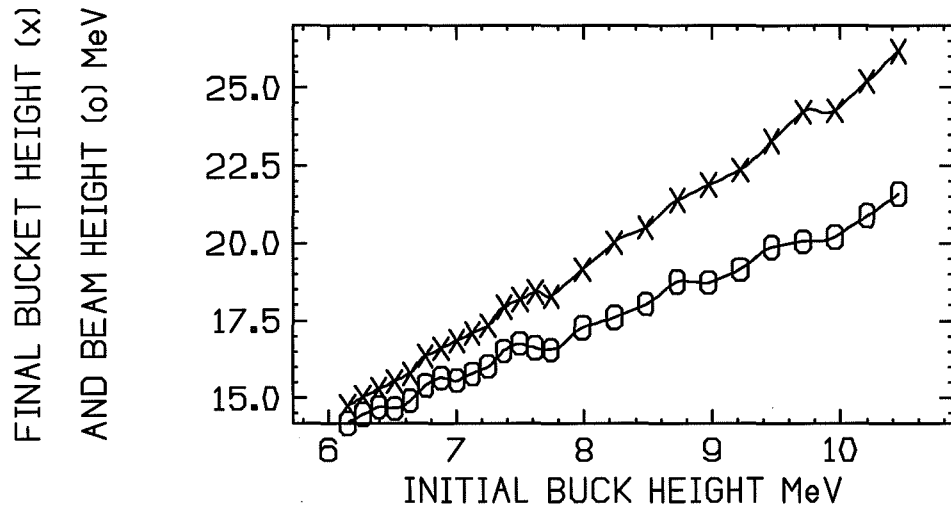


Figure 4. Optimum heights of the final bucket and the beam for various heights of the initial bucket.

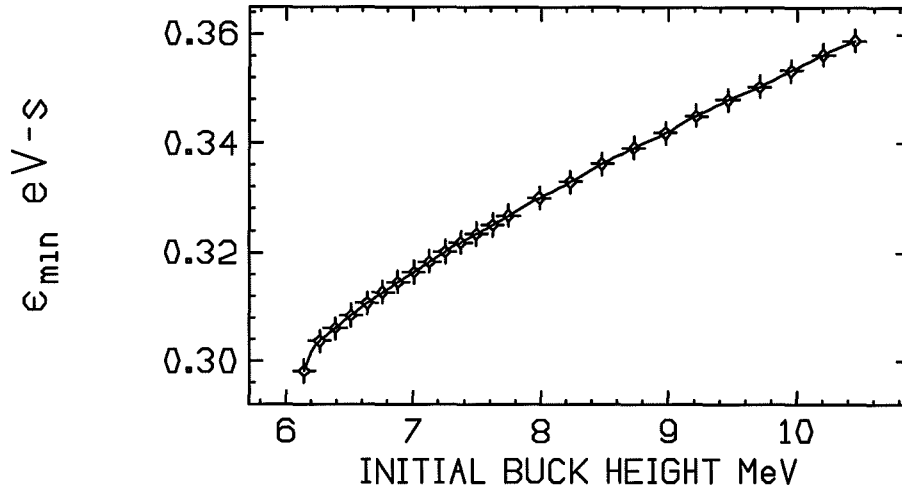


Figure 5. Minimum area containing 95% of beam for various heights of the initial bucket.

### 3.1.3.2 Acceleration and Coalescing

The fractional difference in periods of revolution for the two batches is given by

$$\frac{\Delta T}{T} = \eta \frac{\Delta p}{p}, \quad [6]$$

where  $\Delta p/p$  is the fractional momentum difference and  $\eta$  is the slip factor. The slip factor is given by

$$\eta = \frac{1}{\gamma_t^2} - \frac{1}{\gamma^2} \quad [7]$$

For the MI,  $\gamma_t = 21.8$ ,  $\gamma = 9.55$  at injection, and  $\eta = 8.86 \times 10^{-3}$ . The length of a Booster batch is  $1.57 \mu\text{s}$ , and the period of revolution in MI,  $T = 11.14 \mu\text{s}$  at injection. If the two batches are injected 46 MeV apart and allowed to slip, they would overlap completely after half a Booster cycle, i.e., 33 ms. Simulations show that for a bucket height of 10 MeV, the distortion of the particle distributions due to the presence of the second rf is negligible. However, to obtain a small longitudinal emittance of the final beam, the two beams have to be accelerated towards each other before they are coalesced. The bucket height has to be reduced so that the two beams can be brought close together. Were it not for the effect of the second rf one could accelerate the beams and reduce the bucket height very slowly to minimize particle loss. The presence of the second rf encourages faster rf manipulations once the beams are close to each other.

The rf curve program was determined by trial and error. After a few trials, the variation of the rf voltage, frequency, and synchronous phase angle depicted in Figure 6 was accepted as satisfactory. The two beams are captured with a single rf while they are still accelerating. The efficiency of acceleration and coalescing for a final longitudinal emittance of 0.34 eV-s is 95%. Figure 7 shows the beam distributions just before coalescing along with the initial and final buckets. The dashed curve inside the final bucket is a contour containing 0.34 eV-s of area.

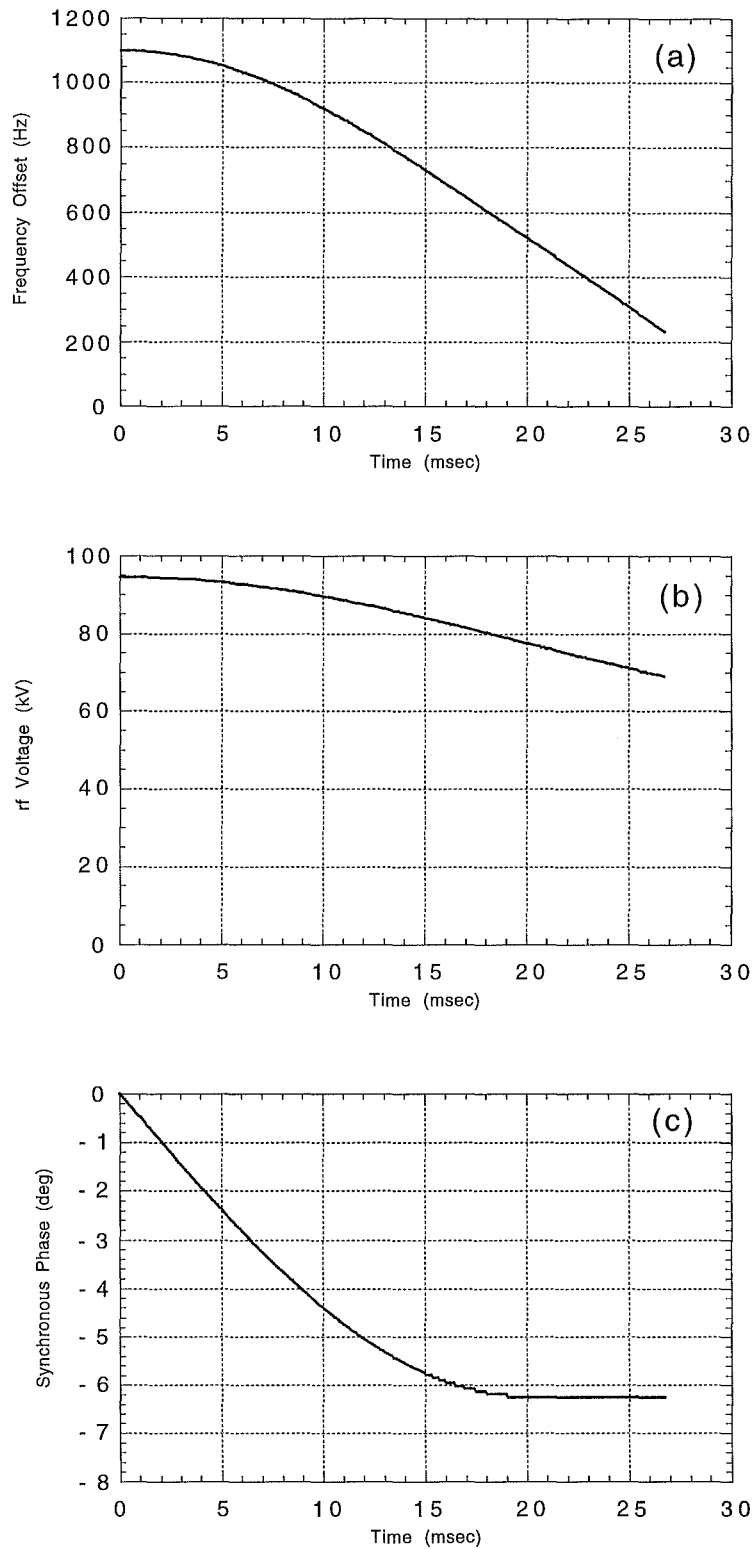


Figure 6. The frequency curve (a), the voltage curve (b), and the resulting synchronous phase angle (c) that were used in the tracking simulation.

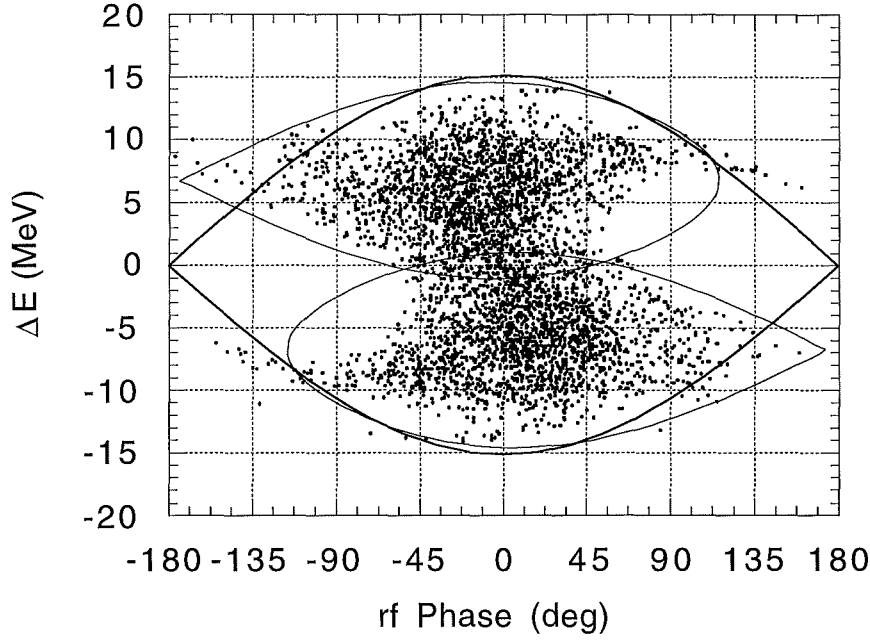


Figure 7 A simulation of slip stacking. The points represent the final phase space coordinates of the particles tracked in the presence of the two rf systems. The smaller curves are the moving rf buckets that would be generated by one system if the other system were not present. The large curve represents the stationary bucket into which most of the particles will be captured.

### 3.1.3.3 Beam Loading

Because of the high beam current, the beam loading voltage in the rf cavities is a serious concern. If the quality factor,  $Q$ , is high and the bunch length is short, the cavity voltage  $V(t)$  following the passage of a bunch of charge  $q$  is given by:

$$V(t) = \frac{q\omega_r R}{Q} e^{-(\alpha+i)\omega_r t} \quad [8]$$

where  $R$  is the cavity shunt impedance,  $\omega_r$  is the cavity resonant frequency, and  $\alpha=1/2Q$ . In the case that the bunches are spaced by  $\tau=2\pi/\omega_r$ , the voltage after the passage of  $n$  bunches is easily found to be

$$V(n\tau) = \frac{q\omega_r R}{Q} \frac{1 - e^{-n\pi\alpha}}{1 - e^{-\pi\alpha}} \quad [9]$$

We can apply Eqn. [9] to estimate the beam loading voltage. As an example, we consider the case where there are two batches of 84 bunches each in the Main Injector and that the last 42

bunches of the first batch and the first 42 bunches of the last batch overlap and are exactly in phase. We ignore the difference in revolution frequencies of the two batches and the difference between the resonance frequency of the cavity and the revolution frequencies. Under these circumstances, one can use a generalization of Eqn. [ 9] to estimate the beam loading voltage as shown in Figure 8. The calculation is for a total of 18 cavities with  $R/Q=100\ \Omega$  and  $Q=5000$ . The voltage increases when the beam passes through the cavities. During the time that the two beams overlap the voltage increases at twice the rate. When the beam is absent the voltage decays at a rate determined by the time constant  $\alpha$ . Approximately 0.4 ms later the bunches are out of phase and the beam voltage becomes very small.

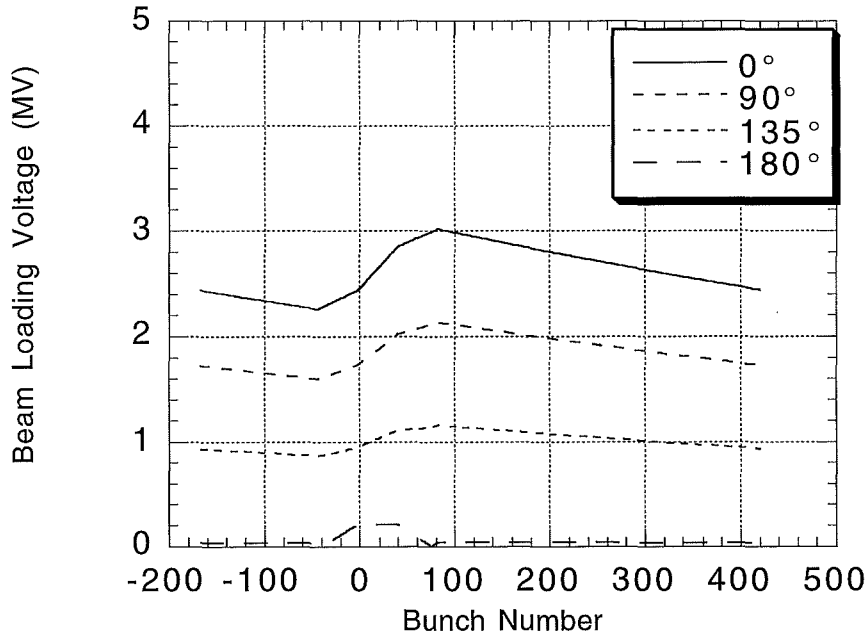


Figure 8. A calculation of beam loading

This estimate of the beam loading voltage indicates that, if uncompensated, the beam loading voltage (3 MV) would dwarf the rf voltage (100 kV). We propose to control the beam loading voltage by:

- 1) Tuning all cavities to the nominal 8 GeV frequency.
- 2) Using a small number of cavities (2 or perhaps 4) to produce the required rf voltage and de-Qing the remaining cavities. One simple technique that appears to be moderately effective is to turn off the screen voltage to reduce the tube plate resistance. This technique is estimated to de-Q the cavities by a factor of 3.
- 3) Feed-forward can be used on all the cavities. A resistive gap measures the wall current. This current, after being properly scaled, can be applied to the cavity

drivers. Based on current Main Ring experience it is expected to achieve a factor of 10 reduction in the effective beam current.

- 4) Feedback can be used on all the cavities. A signal proportional to the gap voltage is amplified, inverted, and applied to the driver amplifier. This technique is expected to achieve a factor of 100 reduction (based on previous experience in the Main Ring and results achieved elsewhere).

If all these efforts were successful, beam loading should be reduced to a negligible value. Experiments in the Main Ring to measure the suppression of the beam loading voltage and calculations of the tolerance of the slip stacking process to large beam loading voltages will determine whether the feasibility of slip stacking in the presence of relatively high impedance rf cavities.

Other collective effects could be important. These include:

- 1) Microwave instabilities at low voltages
- 2) Feedback loop coupling
- 3) Cavity tuning instabilities

We plan further theoretical work and are beginning experimental work using the Main Ring beam.

### **3.2 Antiproton Target**

The higher intensity proton beam expected at the antiproton target in Run II and TeV33 results in an increasingly hostile environment at the target station. Run II doubles the amount of beam targeted; TeV33 results in a further doubling of the intensity. The antiproton source target area is a high radiation area that contains a number of high voltage devices.

#### **3.2.1 Beam sweeping**

One issue that is fairly well understood is the allowable peak energy deposition in solid targets. A sweeping system is envisioned to accommodate the higher intensity in Run II and beyond. The sweeping system is adequate for a doubling of the intensity in TeV33, but higher intensities would require defocusing the beam (and a lower antiproton yield).

Figure 9 shows the scaling of the relative yield of antiprotons as a function of rms beam spot size. Also shown is the energy density in a copper target as a function of rms beam spot size as calculated by MARS10<sup>6</sup> for  $5 \times 10^{12}$  protons per pulse<sup>7</sup>. Estimates of the peak density of energy deposition per pulse achieved to date are in the range of 800 J/g. This is above the melting point of copper (about 600 J/g), and close to the melting point of nickel (about 1000 J/g). In order to maintain peak energy deposition below present levels the spot size would have to be increased to 0.3 mm for Run II ( $5 \times 10^{12}$  protons in a 1.6  $\mu$ s pulse) and the yield would be reduced 15-20% compared to the nominal beam size of 0.10-0.15mm. We plan instead to sweep the beam on the target while synchronously sweeping the downstream acceptance so that we can obtain an effective defocussing of the beam with no reduction in yield.<sup>8</sup> With slip stacking, the sweep radius will need to be increased to about 0.5 mm. The current design of the beam sweeping system will provide a maximum sweep radius of 0.5 mm.

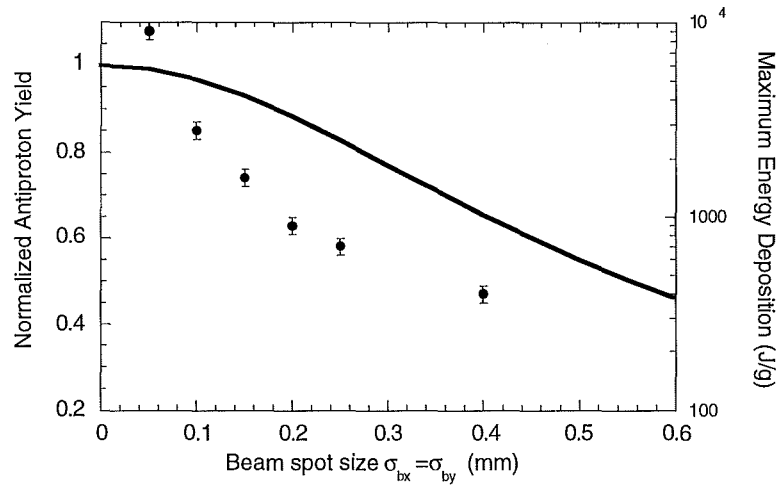


Figure 9. Yield (line) and energy deposition (points) vs. beam spot size

The beam sweeping scheme utilizes two upstream sweep magnets driven in quadrature by a 625 kHz sinusoidal current waveform to trace a circular pattern on the target with the 120-GeV proton beam, followed by two downstream magnets to redirect the 8 GeV antiprotons exiting the collection lens parallel to the AP-2 transport line (see Figure 10). The sweeping radius is much smaller than the 2 cm diameter of the lithium collection lens and the aperture of AP-2. Two current-carrying plates, roughly 3 cm wide, with an air gap of 3 cm, will provide the deflecting magnetic field. An air gap is used since the beam is already transported through air from upstream of the target to downstream of the pulsed magnet. This system is currently an R&D project with expected completion of a prototype kicker magnet and power supply in late 1997.

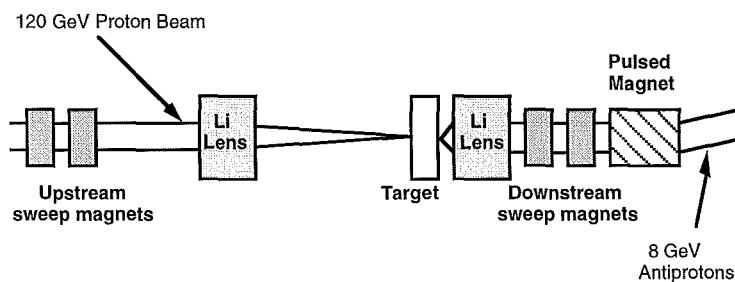


Figure 10. Target station layout showing beam sweeping kicker magnets

### 3.2.2 Lithium lens mechanical issues

The collection lens<sup>9</sup> focuses the antiprotons produced at the target. The effect of the lens gradient on the yield is discussed in section 3.3.1. However, because the lithium lens is subject to the hostile environment encountered in the target station, reliability issues are discussed here. The current-carrying lithium portion has a diameter of 2 cm and a length of 15 cm. The lithium is encased in a cylindrical water-cooled Ti-6Al-4V jacket. Fermilab lithium lenses of recent design have survived over 7 million pulses at a lens gradient of about 750 T/m. Increasing the field gradient of the lens increases the yield. But even a small increase in repetitive stress in the Ti-6Al-4V cylinder (which acts as both a cooling jacket and a pressure vessel) leads to a much shorter fatigue life of the metal. Thus operation at even 5% greater field gradient has not yet proven possible beyond 1-2 million pulses. Several improvements in the design of the lens are expected to further improve reliability and field strength. The goal is reliable operation at 900 T/m. A number of improvements to the mechanical design have been developed. These improvements include thicker endcaps for the cooling jacket, a stronger beryllium window, and improved handling and placement of welds during construction of the cooling jacket. These improvements have been incorporated into the latest lenses and have been operated extensively in the target vault at 750 T/m. It is hoped that they will allow reliable operation at higher lens field gradients in the future.

One particular critical parameter is the lens preload. During the filling process, lithium is pumped under pressure into the evacuated titanium vessel. The preload serves to insure that the lithium cylinder maintains its shape at mid-pulse, when significant magnetic pinch forces are present. Lower preload leads to lower operating stresses; a small stress decrease on the titanium cooling jacket should result in a great increase in the life of the lens for a given field gradient. A recent analysis using ANSYS<sup>10</sup> shows that it is possible to lower the preload pressure in the lithium by at least 15%. The original lens design preload ensured that the lithium would maintain its shape on the first pulse when the lithium is at 20 °C. At steady state, the lens is at 65 °C and the additional thermal stress on the titanium is approximately the same as the stress due to preload. Thus, at steady state almost no preload is needed. If one could reduce the lithium preload from 2300 psi to 500 psi, then the lens would be able to operate at 1000 T/m without deformation of the lithium cylinder. A lens with a preload of 1950 psi is currently in use in the target vault.

Lithium melts at the relatively low temperature of 180 °C. If liquid lithium were used in the lens and circulated through a heat exchanger with a pump, then water cooling of the Ti jacket would not be necessary. This would allow for a much more robust Ti jacket that could withstand much larger shock waves, allowing for larger current pulses and magnetic field gradients. Some R&D has been done in this area in the past.<sup>11</sup> MCLENS calculates that increasing the lens gradient from 900 T/m to 1200 T/m will increase the yield into a  $32\pi \times 32\pi$  aperture by 9%.

### 3.2.3 Radiation damage issues

Information on the maximum allowable radiation dose of insulating materials is sketchy, but we typically exceed the high end of the ranges specified. Because of the large uncertainty in using published data, the final determination on the acceptability of materials for use in our target station will necessarily be based on our experience. Recently, a failure of the torlon<sup>®</sup> insulating material in the "pulsed magnet" was experienced. This material had survived a 4-year beam exposure at current intensities. Higher beam intensities will result in accelerated failure rates or will further restrict the range of materials that can be used in the target vault. Our strategy for TeV33 is to minimize these types of problems by increasing the antiproton acceptance as well as increasing the number of protons targetted.

We have seen a large number of lithium lens failures over the years. Few, if any, of these failures were the result of radiation damage. However, we have realized that the lithium lens is susceptible to a type of radiation damage that is peculiar to the lithium lens. Gaseous products from the reaction  ${}^6\text{Li} + n \rightarrow {}^3\text{H} + {}^4\text{He}$ , are expected to build up over time, possibly affecting the

<sup>®</sup> Torlon is a registered trademark of...



operation of the lens.<sup>12</sup> Swelling of the lens is expected, due to the pressure of the contained gas, potentially limiting the lifetime of the lens under an intense beam environment. To avoid this problem, we have identified a source of 99% isotopically pure <sup>7</sup>Li and are currently building all lenses with this material.

### 3.2.4 Antiproton target radiation shielding and environmental issues

The radiation shielding and environmental issues are fairly well understood. Higher beam intensities will probably require modifications to the shielding or to the accessibility of the target hall. It is likely that improved air handling procedures (to reduce airborne contamination) will also be required. Some of the major concerns are listed below.

- 1) The target vault is classified as a high radiation area (<100 mrem/hr). Some additional concrete may be required to maintain this classification (0.5 m of concrete→factor of 2 reduction in radiation).
- 2) The APO building is classified as a radiation area (<10 mrem/hr). Some additional concrete shielding may be required to maintain this classification. As an alternative, some critical areas could be roped-off.
- 3) Water system
- 4) Stairwells and penetrations have not been considered in detail, but may need some additional shielding measures.
- 5) Some additional soil may be required over the beamlines.
- 6) The ground water contamination potential has been considered with the "Concentration Model." The result of the calculation based on this model is that we can target  $10^{22}$  protons per year in the antiproton target station. This is well within the TeV33 parameters of  $10^7$  pulses of  $10^{12}$  protons per pulse.
- 7) The limit on airborne emissions is 100 Ci per year. The measured<sup>†</sup> target station emissions indicate that  $10^{20}$  protons per year will saturate the 100 Ci limit.

### 3.2.5 Antiproton Target Conclusions

In summary, our current understanding is that targeting twice the Main Injector intensity (*i.e.*,  $10^{13}$  per batch) is technically feasible provided that the beam sweeping system operates reliably.

## 3.3 Antiproton Acceptance

We plan to increase the antiproton acceptance by increasing the gradient at which the lithium lens can reliably operate and by increasing both the transverse and longitudinal acceptance in the Debuncher. Increasing the acceptance has the advantage that it makes no new requirements on the proton beam and target station components, but it has the disadvantage that a larger phase space area must be cooled.

### 3.3.1 Lithium Lens Gradient

Measurements of yield vs. gradient (Figure 11) show that a 17% increase in yield is obtained at 900 T/m compared to 750 T/m. We have established a goal of 900 T/m for the improved lithium lens design described in section 3.2.2. A Monte Carlo calculation (MCLENS<sup>13</sup>)

---

<sup>†</sup>In 1995 (a collider run)  $15 \times 10^{18}$  protons were targetted and 19 Ci were released.

indicates that an additional 11% increase in yield is obtained for a 900 T/m lens if AP-2 line is reoptimized for an initial phase space ellipse of  $\beta=3.1\text{m}$ . The overall increase to a 900 T/m lens and optimized AP-2 line is thus 30%.

*[Editors note: Seems like something is inconsistent here. We quoted 11% improvement in Table V. I changed the above to say we get 17% $\times$ 11%. Was the 17% included elsewhere?]*

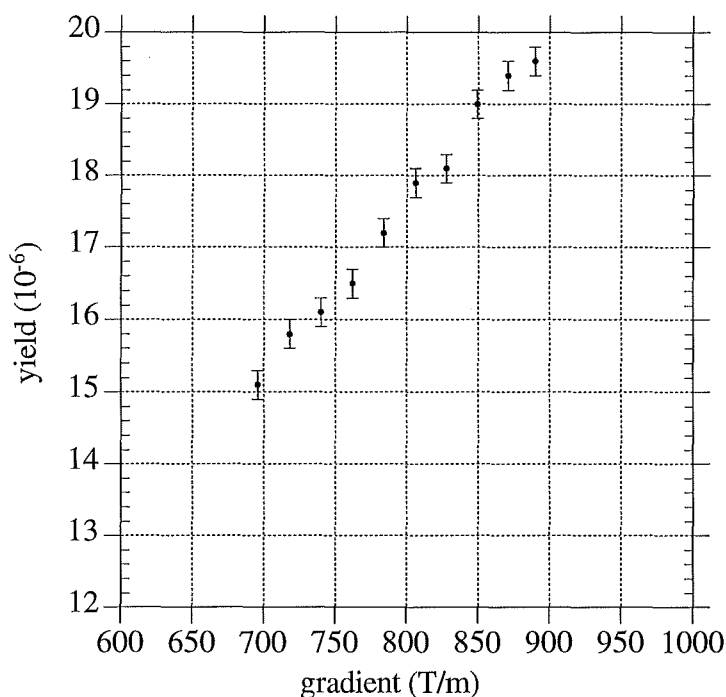


Figure 11. Measured yield vs. lithium lens gradient

### 3.3.2 Transverse aperture increase to $32\pi \times 32\pi$

The transverse phase space area of antiprotons accepted into the Debuncher during stacking has been measured to be  $15\pi \times 16\pi$  (see Figure 12). This is substantially smaller than the measured admittance of the Debuncher of  $29\pi \times 26\pi$ , and we have concluded that the AP-2 beam transport line is limiting the acceptance. Recently, the quadrupoles in the upstream end of AP-2 were surveyed and realigned in an effort to minimize quadrupole steering, however, no increase in yield was observed. Work is presently underway to develop an accurate beam line model and improve the beam line tune, steering, and matching into the Debuncher.

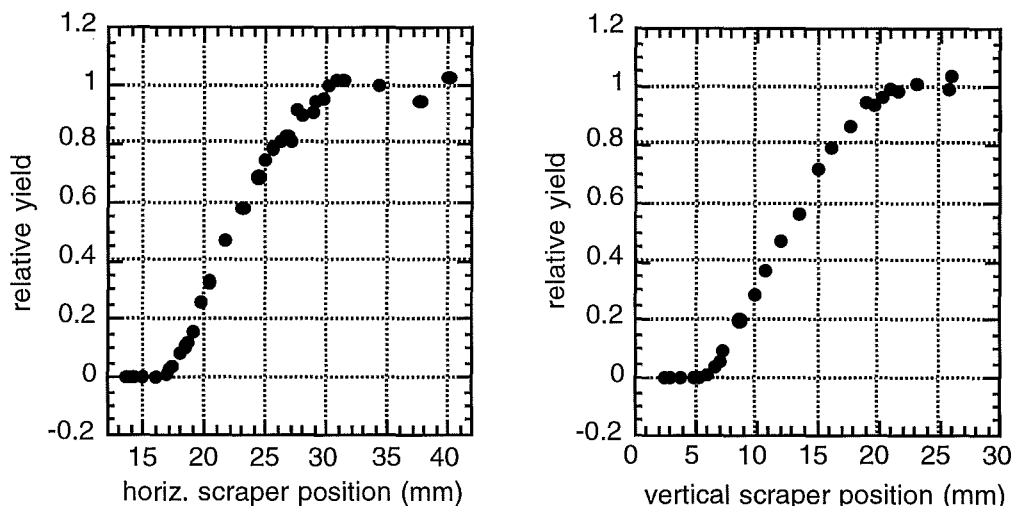


Figure 12. The transverse phase space area of antiprotons circulating in the Debuncher is deduced by measuring yield versus transverse scraper position and using  $A=\Delta x^2/\beta$ . At the location of the scrapers,  $\beta_x=13.1\text{m}$  and  $\beta_y=13.9\text{m}$ .

Figure 13 shows a Monte Carlo simulation<sup>14</sup> (using the computer program MCLENS<sup>15</sup>) of the antiproton phase space density in the horizontal dimension at the downstream focus of the lithium lens. A fit to measured yield vs. target-to-lens distance indicates that the aspect ratio of the phase space ellipse at the lens which is accepted into the Debuncher is now  $\beta=2.5\text{m}$  horizontally and  $\beta=1.5\text{m}$  vertically.<sup>16</sup> However, for apertures up to about  $32\pi \times 32\pi$  and for a lens gradient of  $750\text{ T/m}$  the optimum phase space ellipse (maximum yield) is  $\beta=4.5\text{m}$  in both dimensions. If AP-2 can be retuned to inject this phase space into the Debuncher, the yield will increase by a factor of 2.59 at the current lens gradient, according to the above Monte Carlo calculation. A major uncertainty in this extrapolation is the assumption that the current acceptance is an ellipse centered in phase space. (There is no reason it must be.) Figure 14 shows the beam envelope for  $32\pi \times 32\pi$  beam, initial  $\beta_{x,y}=4.5\text{m}$ , and  $\Delta p/p=4\%$  in an AP-2 model. This model (assuming perfect steering) shows that the beam easily fits in the AP-2 beampipe, except possibly at the injection septum. For this particular model, the narrowest apertures are horizontally at the upstream end of the septum ( $4.2 \times$  beam sigma), vertically at the downstream end of the septum ( $6.5 \times$  beam sigma), and horizontally at the upstream end of the injection kicker ( $6.7 \times$  beam sigma).

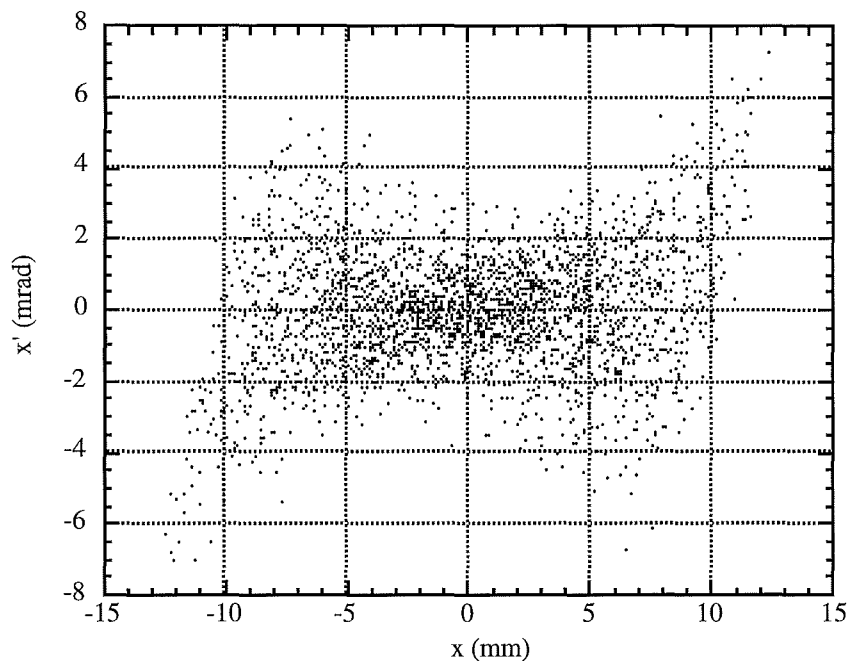


Figure 13. Calculated phase space density at the downstream focus of the lithium lens with a lens gradient of 750 T/m. Vertical dimension is the same due to cylindrical symmetry.

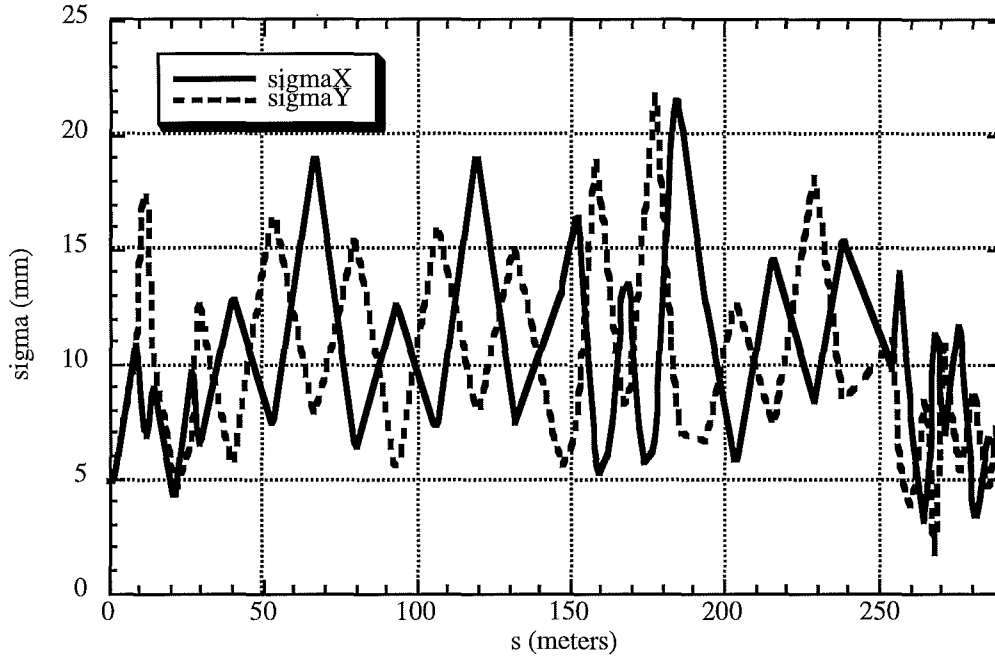


Figure 14. Vertical and horizontal beam envelopes in AP-2 based on model with  $32\pi \times 32\pi$  beam, initial  $\beta_{x,y}=4.5\text{m}$ , and  $\Delta p/p=4\%$ . Left side of figure is downstream focus of lithium lens, and right side of figure is downstream end of Debuncher injection kicker magnet.

The Debuncher transverse aperture has been measured to be  $29\pi \times 26\pi$  at  $\Delta p=0$ , although after optimization of the aperture it generally deteriorates over a period of time to something more like  $25\pi \times 23\pi$ . Aperture scans indicate that the limitations are at the stochastic cooling pickup and kicker arrays. The Debuncher stochastic cooling upgrade for Collider Run II will make use of plunging pickup and kicker arrays, which open to an aperture of  $40\pi$  at injection and then plunge inward following the beam profile during the cooling cycle. Studies done in the past<sup>17</sup> found that even with the cooling tanks removed, the apertures were still limited to about  $29\pi$  (at  $\Delta p=0$ ). The Debuncher model indicates (ignoring focussing errors) that without the cooling tanks, the aperture is greater than  $40\pi$  everywhere except at the extraction kicker ( $A_y=36\pi$ ) and the injection septum ( $A_y=29\pi$ ). A stronger injection kicker would allow for a greater separation between the circulating beam and injected beam at the downstream end of the septum. Then, bumping the closed orbit away from the septum would allow for a vertical aperture larger than  $40\pi$  at that point. The issue of whether or not new kickers are required needs more careful study. A further possible cause of the limited aperture is quadrupole misalignment, which causes beam steering, which cannot be corrected because there are very few correction elements in the bend sections of the Debuncher. Figure 15 summarizes a recent Debuncher quadrupole survey. These elements will be realigned during the long shutdown for Main Injector installation. If this does not open up the aperture, then a program of installing motorized quadrupole mounts, dipole shunts, and possibly trim elements needs to be initiated in order to obtain an acceptance of  $32\pi \times 32\pi$  mm-mrad.

The Debuncher transverse aperture is smaller at values of  $\Delta p \neq 0$ . In yield calculations it is assumed that if the transverse aperture at  $\Delta p = 0$  is increased by a multiplicative factor, the aperture at  $\Delta p \neq 0$  will increase by that same multiplicative factor.

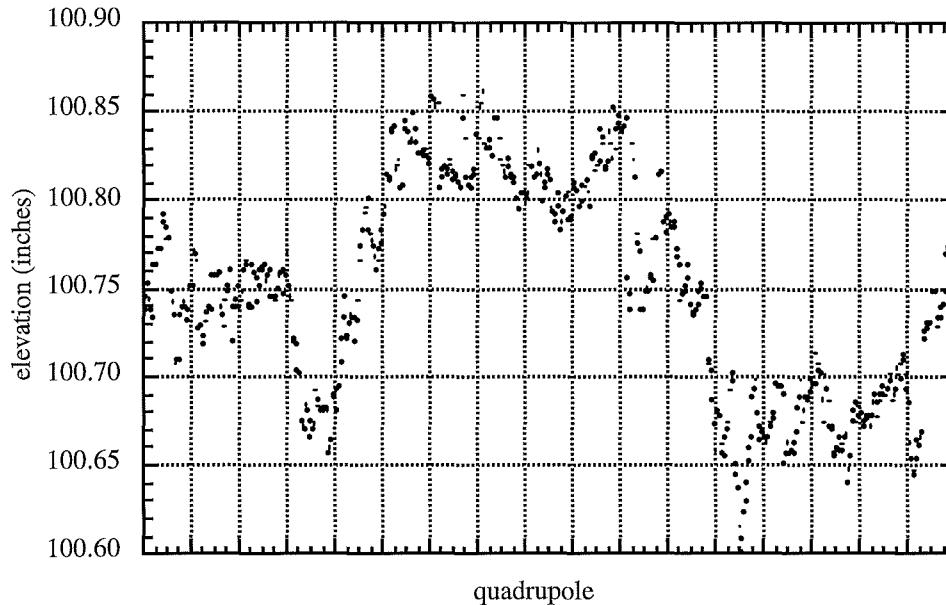


Figure 15. Quadrupole vertical misalignment in the Debuncher Ring. Each quadrupole was surveyed at its upstream end and downstream end.

### 3.3.3 Momentum aperture increase

By decreasing the slip factor  $\eta$  in the Debuncher from its design value of .006 to .003 at injection time, the momentum aperture of the Debuncher can be increased by 18% at injection. This is accomplished by reducing the dispersion in the bend sections of the Debuncher. Figure 16 shows the dispersion function in the Debuncher for 2 different values of  $\eta$ . The  $\eta$  change is implemented in the lattice with a series of overlapping local dispersion bumps in the high dispersion regions which reduce the dispersion there. After bunch rotation and adiabatic debunching, which occurs in the first 60 msec of the beam cycle,  $\eta$  will be ramped to .009 to improve stochastic cooling. A ramp from .006 to .009 has already been successfully tested in the Debuncher,<sup>18</sup> although some work is still required on the Debuncher quadrupole power supply regulation circuits and quadrupole shunt circuits to improve tune control and prevent crossing resonance lines during a fast ramp. This ramp does not change the beta functions anywhere in the ring by more than 5%.

The current momentum aperture of the AP-2 left bend is at least 4%. The limitation is the dispersion in the left bend, where the beam is scraped from nominally  $\Delta p/p = 10\%$  to  $\Delta p/p = 4\%$ . The question of whether the AP-2 beamline will need to be modified to accommodate an 18% larger momentum spread needs to be investigated experimentally.

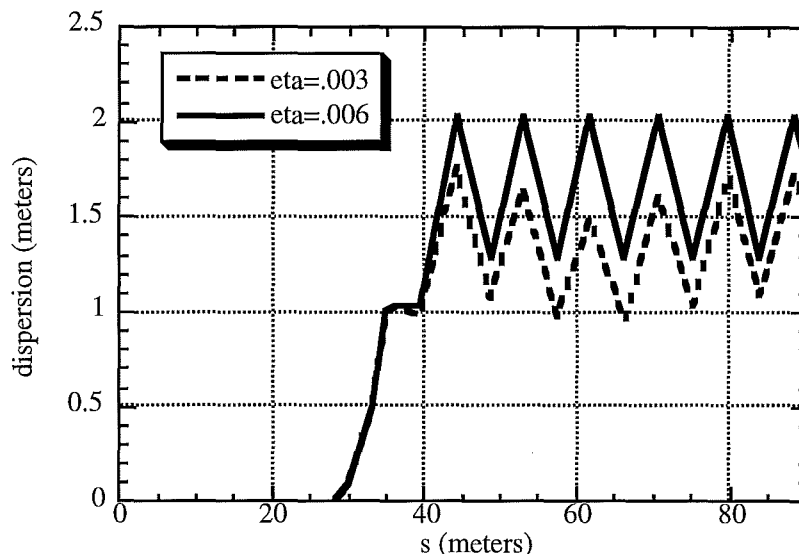


Figure 16. Dispersion function in the Debuncher for 2 different values of  $\eta$ ; the 18% increase in momentum aperture comes from the ratio of the maximum dispersion for the  $\eta=.003$  lattice and the  $\eta=.006$  lattice.

### 3.4 Antiproton Bunch Rotation

Bunch rotation is a crucial emittance preservation technique that is used in the production of antiprotons. The effectiveness of the bunch rotation depends on the longitudinal proton emittance in the Main Injector. The process has been simulated using the existing 5 MV rf system and an initial antiproton momentum spread of  $\pm 2.4\%$ . The final momentum spread of the antiprotons versus the initial proton longitudinal emittance is shown in Figure 17. For larger longitudinal emittances the Debuncher momentum spread depends linearly on the initial time spread in the proton beam. For very small emittance, non-linearities in the bunch rotation process are responsible for the final momentum spread. In this case, the momentum spread can be reduced by using a higher harmonic rf system in the Debuncher. Figure 17 also shows the momentum spread of the Debuncher beam measured in Run Ib and the bunch lengths expected in the Main Injector for longitudinal emittances of 0.15 eV-sec (nominal Main Injector emittance) and 0.5 eV-sec (slip stacking goal).

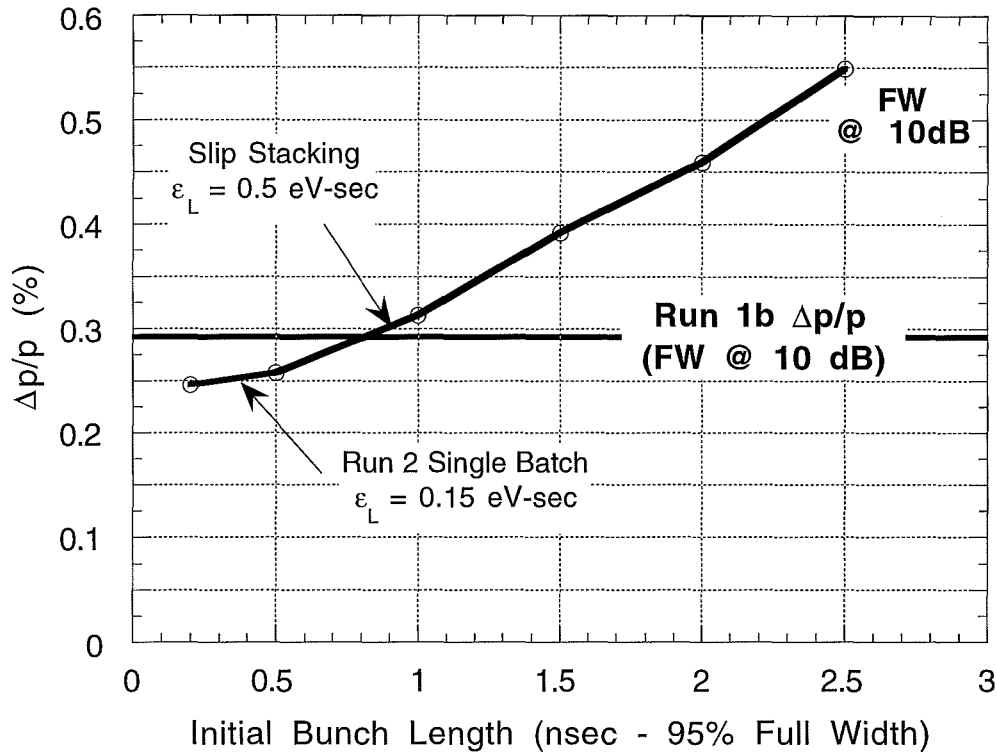


Figure 17. Bunch rotation momentum spread versus initial bunch length.

### 3.5 Antiproton Cooling Overview

For Run II, an upgrade of the existing 2-4 GHz cooling system in the Debuncher and an upgrade the 1-2 GHz stack tail cooling system to a 2-4 GHz cooling system will support stacking rates of  $2 \times 10^{11}$ /hour for Run II. . We plan to use stochastic cooling in the Recycler initially as described in the Recycler Design Handbook (see ref. 3).

An additional factor of 4 increase in antiproton flux can be accommodated by additional upgrades in the Debuncher and the Accumulator to 4-8 GHz. The Debuncher systems would achieve the factor of 4 increase in cooling rate by doubling the bandwidth (a factor of 2) and by reducing the mixing factor (the second factor of 2). The stack tail system in the Accumulator would benefit from an increased bandwidth (a factor of 2), but would have half its cooling load assumed by the Recycler Ring. An important ingredient of this effort is an R&D effort to produce high sensitivity 4-8 GHz pickups and kickers.

In the Recycler an electron cooling system will be used to longitudinally stack the antiprotons for TeV33. Electron cooling promises much higher cooling rates than would be possible with the multi-GHz stochastic cooling systems used in the Debuncher and Accumulator rings. Stochastic cooling rates are inversely proportional to the number of particles being cooled while electron cooling is independent of the number of particles to be cooled. The high beam intensities in the Recycler favor electron cooling by a wide margin. The rf manipulations and beam transfers are not described in this report but are essentially identical to those described in the Recycler Design Report (see ref. 3) and the Tevatron I Design Report.<sup>19</sup>



The cooling calculations assume that  $6 \times 10^8$  antiprotons are delivered at 2 sec intervals to the Debuncher in 1 nsec bunches with a full (100%) momentum  $\Delta p/p = 4.8\%$  and a transverse emittance (100%) in each plane of  $\epsilon = 32 \pi$  mm-mrad. The beam is debunched to momentum spread of 0.3% and cooled to 0.2%. The beam is cooled by about a factor of 4 transversely to  $6 \pi$  mm-mrad. Table VI summarizes the beam parameters in the Debuncher.

Table VI. Summary of Beam Parameters for Debuncher Cooling

Injected Beam Parameters		
Intensity	$6.0 \times 10^8$	
Bunched Momentum Spread (full)	4.8	%
Debunched Momentum Spread (full)	0.3	%
Transverse Emittance (100%)	32	$\pi$ mm-mrad
Extracted Beam Parameters		
Intensity	$5.8 \times 10^8$	
Momentum Spread	0.2	%
Transverse Emittance (95%)	6	$\pi$ mm-mrad
Injection Repitition Period	2	sec
Extraction Repitition Period	2	sec

The beam is transferred to the accumulator ring where it is stacked longitudinally and cooled transversely by a factor of 7. Every 60 sec the most dense 8 eV-sec of longitudinal phase space is transferred to the Recycler. The frequency of transfers and the size of the longitudinal emittance depend on the performance of the cooling systems in the Recycler and the Accumulator, and will probably be adjusted in the future. The Accumulator beam parameters are shown in Table VII.

Table VII. Summary of Beam Parameters for Accumulator Cooling

Injected Beam Parameters		
Intensity	$5.6 \times 10^8$	
Momentum Spread	0.2	%
Transverse Emittance (100%)	7	$\pi$ mm-mrad
Extracted Beam Parameters		
Intensity	$1.6 \times 10^{10}$	
Momentum Spread	0.06	%
Longitudinal emittance	8	eV-sec
Transverse Emittance	1	$\pi$ mm-mrad
Injection Repitition Period	2	sec
Extraction Repitition Period	60	sec

The beam is stacked longitudinally in the Recycler with electron cooling. The nominal stacking cycle is 60 sec, but this time can be varied according to the strength of the electron cooling

and the ability of the Accumulator to store beam. The projected Recycler beam emittance shown in Table VII are upper limits, but are anyway smaller than the parameters required for the Tevatron beam parameters (Table II). The smaller emittance, if preserved to low beta, will produce a higher luminosity than those shown in the table. On the other hand, the emittance could be intentionally diluted to avoid instabilities if necessary.

Table VIII. Summary of Beam Parameters for Recycler Cooling

Injected Beam Parameters		
Intensity	$5.6 \times 10^8$	
Longitudinal Emittance	8	eV-sec
Transverse Emittance (100%)	1	$\pi$ mm-mrad
Extracted Beam Parameters		
Intensity/bunch	$27 \times 10^{10}$	
Longitudinal Emittance/bunch	$< 0.5$	eV-sec
Transverse Emittance	$< 1$	$\pi$ mm-mrad
Injection Repetition Period	60	sec
Extraction Repetition Period	$\sim 4.0 \times 10^4$	sec

### 3.6 Transverse Cooling in the Debuncher

The beam is cooled transversely in the Debuncher by a conventional stochastic cooling system. The process has been simulated by a computer program that is similar to the one used to design the present Debuncher cooling system. This computer program comprehensively describes the stochastic cooling process by solving a Fokker-Planck equation for the beam distribution as a function of betatron amplitude. The solution includes the effects of good and bad mixing, thermal noise, and signal suppression. The initial and final beam distribution functions are shown in Figure 18. Figure 18 also illustrates the distribution that would be obtained with half the cooling power.

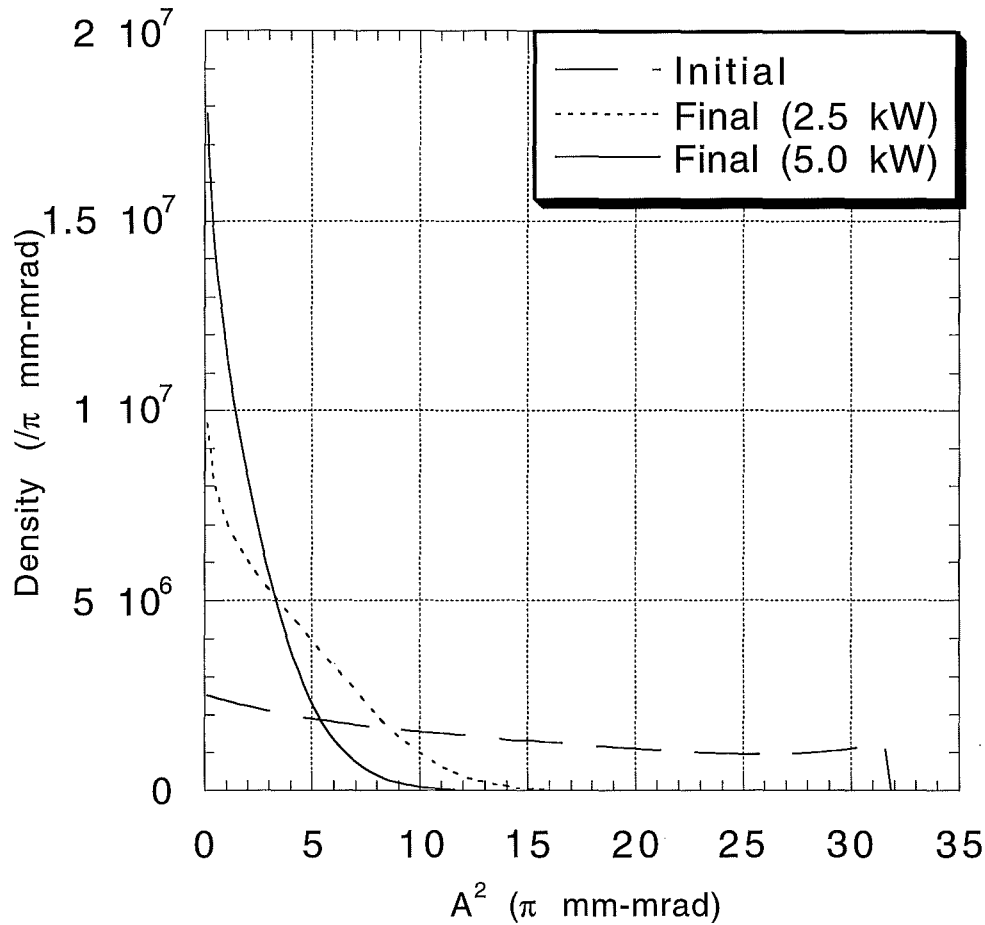


Figure 18. Debuncher transverse cooling simulation.

Since broadband microwave power is expensive, it is important that the power level be kept as low as possible. One of the largest uncertainties in the determination of the required power level is the coupling of the kicker power to the beam. For the purposes of the calculation, a model of an array of strip-line pickups and kickers has been used. The structure actually used will be determined by the 4-8 GHz pickup and kicker R&D program that is described in 3.9.1. It has been assumed that the pickups and kickers are of the "plunging" type: and that the aperture is continuously adjusted to maximize the cooling rate while minimizing the loss of particles from scraping on the pickups and kickers. If the impedance is sufficiently high, it may not be necessary to utilize plunging pickups. The parameters of the beam and the cooling system are given in Table IX.

Table IX. Debuncher Transverse Cooling Parameters.

Number of particles	$6 \times 10^8$	
Efficiency	93	%
Cycle time	2	sec
Initial emittance	32	$\pi$ mm-mrad
Final emittance (95%)	6	$\pi$ mm-mrad
Frequency Band	4-8	GHz
Number of PU's	128	
PU impedance	50	$\Omega$
PU sensitivity	0.8	
PU noise temperature	20	$^{\circ}\text{K}$
Amplifier noise temperature	40	$^{\circ}\text{K}$
Electronic gain	145	dB
PU loss factor	0.70-0.77	
Number of Kickers	128	
Kicker impedance	50	$\Omega$
Kicker sensitivity	0.8	
Kicker loss factor	0.65-0.75	
Thermal noise power	1.1	kW
Schottky noise power	3.9	kW
Total power	5.0	kW

The cooling system described above provides nearly  $10\times$  the cooling rate as the system described in the Tevatron I Project Design Report. The major reasons for the improved capability are given in Table X.

Table X. Comparison of the Tevatron I Project and the Proposed Design

Item	Tev I	Tev33	Improvement
Bandwidth	2-4	4-8	2
$\eta = 1/\gamma_i^2 - 1/\gamma^2$	.006	.009	1.5
Mixing	10	5	2
Power (W)	1000	5000	2
Total			12

### 3.7 Debuncher Momentum Cooling

The Debuncher momentum cooling will be similarly improved by using the 4-8 GHz band. The momentum cooling uses the same pickups and kickers and the transverse cooling system. It only requires additional electronics: low noise amplifiers, medium level electronics including a notch filter, and additional traveling-wave tube (TWT) power amplifiers. None of these components present additional challenges beyond those described in the section on Debuncher Transverse Cooling. The performance requirements for momentum cooling are lower (cooling by less than a factor of 2) and the signal to noise ratio is better because the longitudinal signal is

stronger than the transverse signal and because the momentum system uses pickups from both the horizontal and vertical systems.

The performance of the upgraded simulation is illustrated in Figure 19. Momentum cooling in the Debuncher is useful, but it is not critical with our current operating parameters and it is not expected to be critical for TeV33. Under current operating conditions, momentum cooling increases the accumulation rate by about 30%. The size of the increase depends of the momentum spread obtained from the bunch rotation and may be different with the Main Injector. The cooling system parameters used in the simulation are given in Table XI.

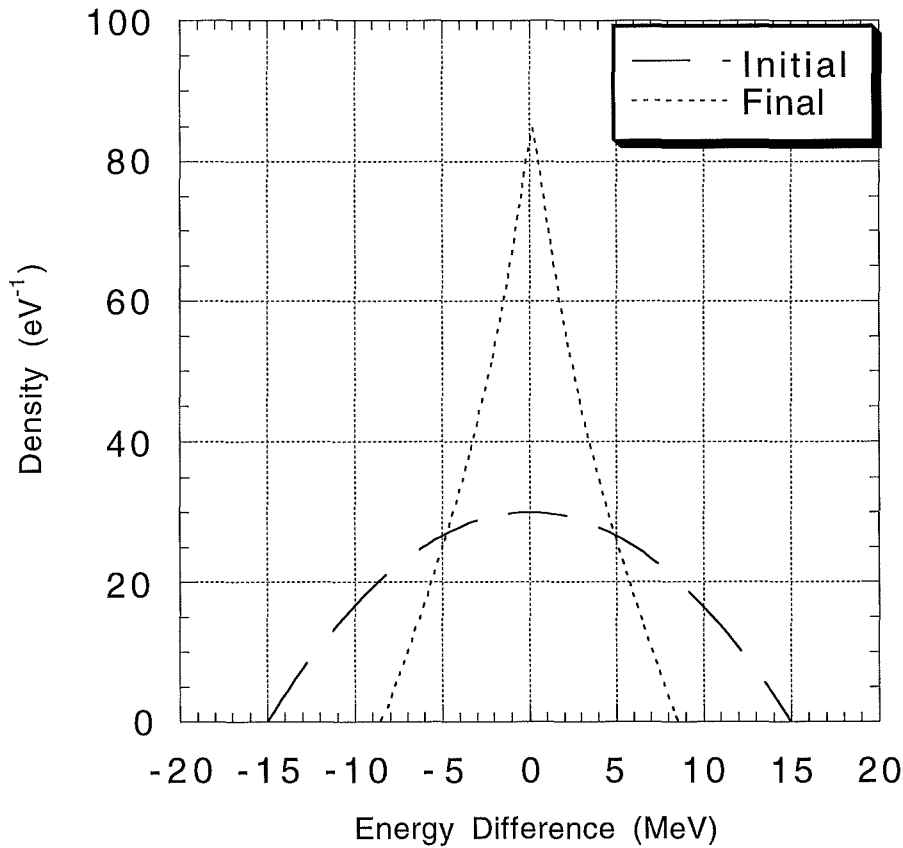


Figure 19. Simulation of momentum cooling in the Debuncher.

Table XI. Debuncher Momentum Cooling Parameters.

Number of particles	6×10 <sup>8</sup>	
Efficiency	100	%
Cycle time	2	sec
Initial Momentum Spread (full)	30	MeV
Final Momentum Spread (full)	11	MeV
Frequency Band	4-8	GHz
Number of PU's	256	
PU impedance	50	Ω
PU sensitivity	0.7	
PU noise temperature	20	°K
Amplifier noise temperature	40	°K
Electronic gain	140	dB
Number of Kickers	256	
Kicker impedance	50	Ω
Kicker sensitivity	0.7	
Thermal noise power	110	W
Schottky noise power	370	W
Total power	480	W

### 3.8 Longitudinal Stacking in the Accumulator

The TeV33 longitudinal stacking system is similar in concept to the current stacktail system. A major design consideration is the amount of cooling done. A model, due to van der Meer,<sup>20</sup> relates the rate of accumulation of flux ( $\Phi$ ) to other system parameters

$$\Phi = - \frac{TW^2|\eta|}{p\Lambda E_d} \quad [10]$$

where  $W$  is the cooling system bandwidth,  $T$  is the revolution period of the storage ring,  $\eta = 1/\gamma_t^2 - 1/\gamma^2$ ,  $p$  is the nominal beam momentum,  $\Lambda$  is a numerical factor  $\Lambda = \ln 2$ , and  $E_d$  is the logarithmic slope of the density distribution  $\Psi(E)$ :

$$\frac{1}{E_d} = \frac{1}{\Psi} \left| \frac{d\Psi}{dE} \right| \quad [11]$$

where  $\Psi(E)$  is the particle density distribution. With the other parameters fixed, an arbitrarily large antiproton flux can be accommodated in the accumulator by tailoring the logarithmic slope of the gain to arbitrarily small values. The consequence of small values of  $E_d$  is that less cooling is done in the Accumulator. The cooling deficit (compare to the Run I and Run II designs) will be absorbed by the electron cooling system that will be available in the Recycler as discussed in section 3.10.

The system contains pickups in the high dispersion regions of the Accumulator, correlator notch filters, and kickers in 0 dispersion. The stacking process has been simulated by a computer program that is similar to the one used to design the Debuncher momentum cooling system and the

Stack Tail momentum cooling system in the Accumulator. A tutorial description of this process was given in the Tevatron Project I Design Report (see reference 19). The computer program comprehensively describes the stochastic stacking process by solving a Fokker-Planck equation for the distribution function. A block diagram of the system is shown in Figure 20.

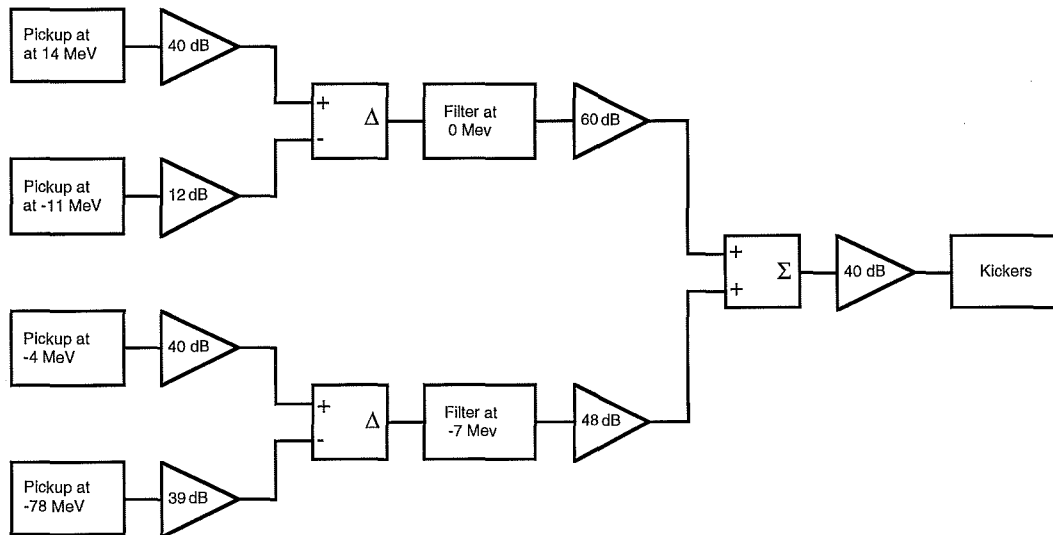


Figure 20. Block diagram of the TeV33 stack tail cooling system.

It is planned that beam would be stacked in the Accumulator for 60 sec. After this interval, the beam would be extracted and transferred to the Recycler Ring. Figure 21 shows the antiproton energy density function at 0 sec (immediately following a transfer to the recycler) and after 20 and 40 seconds of stacking. The parameters of the beam and the cooling system are given in Table XII.

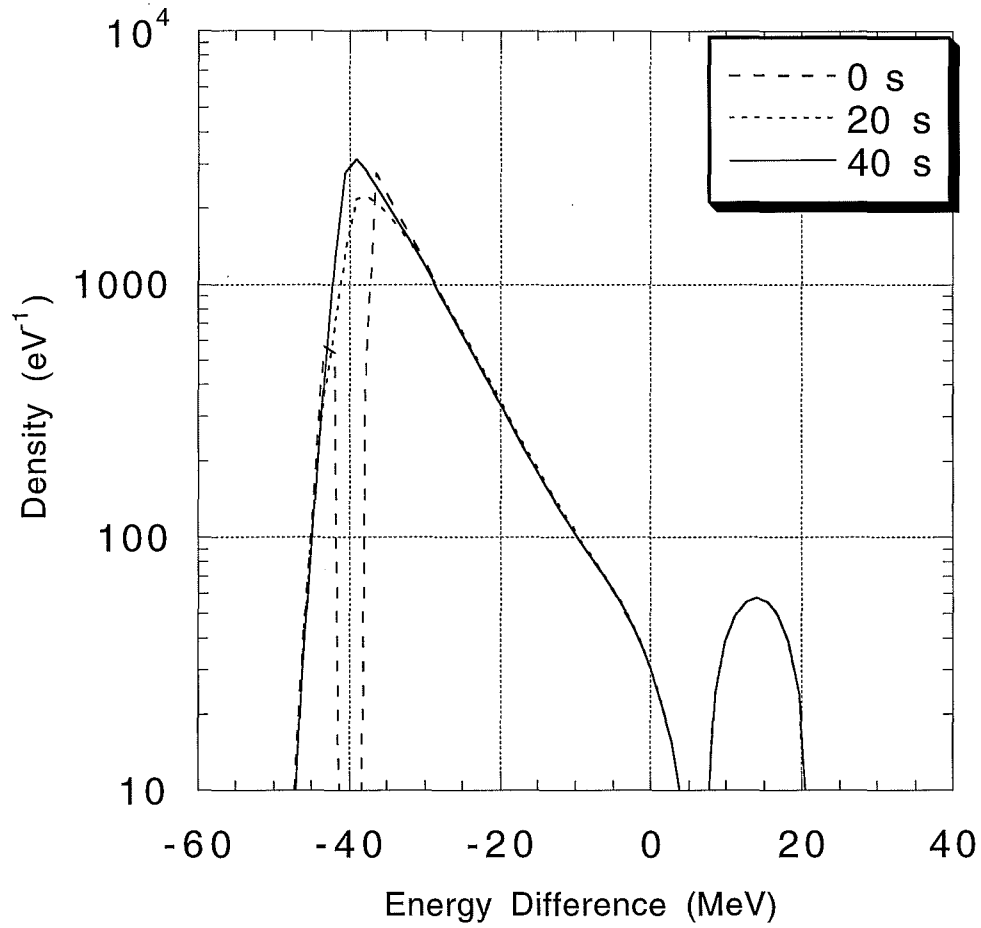


Figure 21. Simulation of Accumulator Stacking.



Table XII. The Accumulator Stochastic Stacking System Parameters

Number of particles	5.6×10 <sup>8</sup>	
Stacking Efficiency	99	%
Cycle time	2	sec
Initial density	57	eV <sup>-1</sup>
Final density	3200	eV <sup>-1</sup>
Final ΔE	5	MeV
Frequency Band	4-8	GHz
Number of PU's	128	
PU impedance	50	Ω
PU sensitivity	0.7	
PU noise temperature	40	°K
Amplifier noise temperature	40	°K
Number of Kickers	128	
Kicker impedance	50	Ω
Kicker sensitivity	0.7	
Thermal noise power	150	W
Schottky noise power	1800	W
Total power	1950	W

### 3.9 Stochastic Cooling Technology

As discussed above there are two technologies that are crucial to the success of these upgrades. The first technology is the 4-8 GHz pick-up and kicker loops. The second technology is signal transmission which we intend to base on a laser modulation/demodulation scheme. Other technologies including microwave components and amplifiers are commercially available for the 4-8 GHz band.

#### 3.9.1 4-8 Ghz Pickups

Present Stochastic Cooling Electrode technology is based on octave bandwidth planar loops. The gain of these falls off quickly at high frequencies. For example, a 100Ω characteristic strip-line loop has a measured sensitivity of 3Ω at 2-4 Ghz. A similar 100Ω loop has a measured sensitivity of 0.75Ω at 4-8 Ghz.

Many of these low sensitivity broadband loops are combined in binary arrays to form a broadband array. There are a number of problems with binary combiner boards. Even at 2-4 Ghz, they may have large insertion losses and microwave modes. Also, microstrip combiner boards have large line to line coupling which require large boards which is inefficient for cryogenics. Although stripline is electrically superior to microstrip it is much more difficult to deal with mechanically

However, 4-8 GHz slots, have been measured to be more sensitive than 3-D loops or planar loops. A single waveguide slot has been calculated to have an effective impedance of 37 Ω over a bandwidth of 0.7 GHz at 6 Ghz as shown in Figure 22. The slot couples electromagnetic energy from the wakefield of the beam into the output waveguides as shown in Figure 23. The energy of a number of slots can be added together constructively if the phase velocity of the wave in the outer waveguides matches the velocity of the beam. A waveguide without any slots has a phase velocity faster than the velocity of light. The slots act to "slow down" the phase wave in the

outer waveguides. The number of slots per length will determine the phase velocity of the wave in the outer waveguides. Research has been started to calculate what line density of slots is needed to match phase velocities. This type of structure is commonly known as a slow wave Floquet structure. This structure is also similar in concept to the 8-10 GHz CERN design of the slow wave ridged pickup array used for bunched beam cooling.

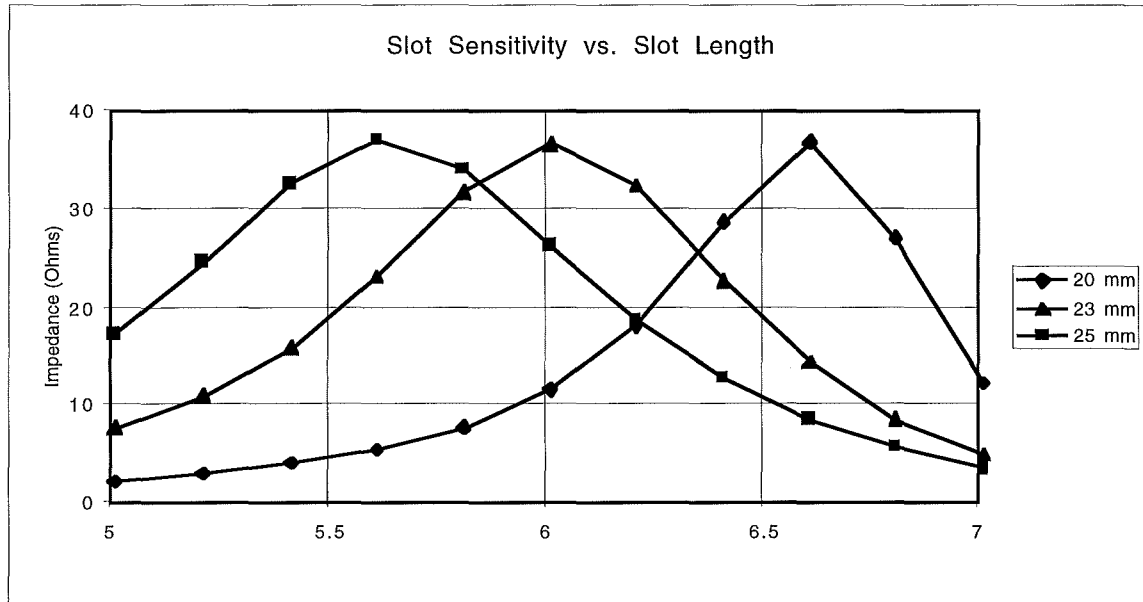


Figure 22. Coupling impedance versus frequency for an single slot of varying width..

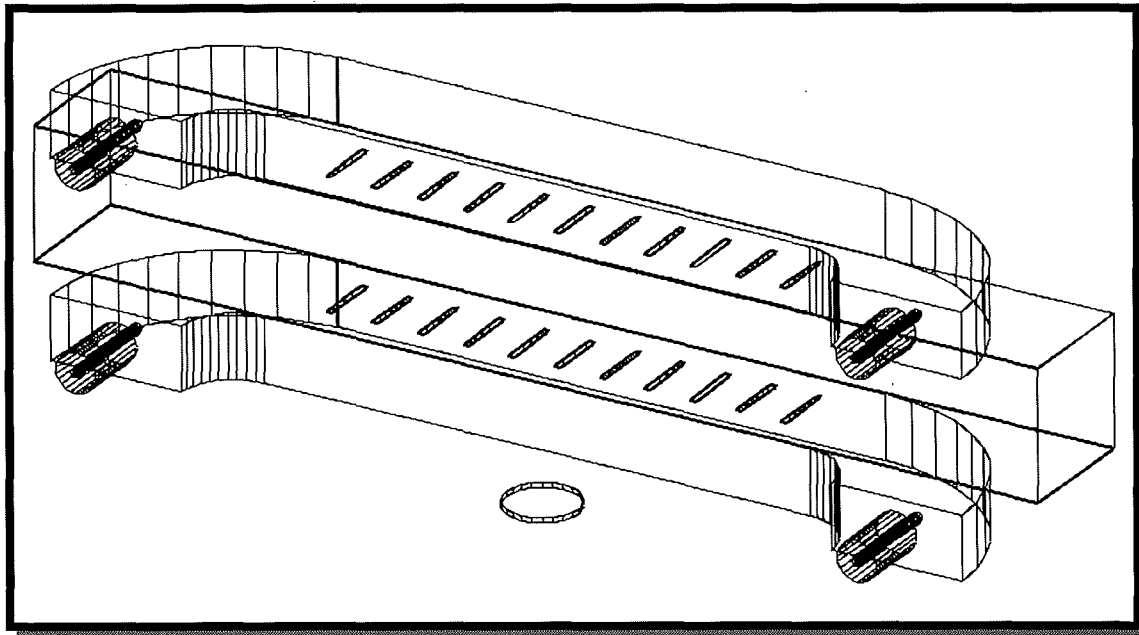


Figure 23. A conceptual drawing of a 4-8 GHz slot array.

Each slot array will be narrowband ( $<1.0\text{GHz}$ ) but tuned to a separate center frequency. The arrays will be summed together to form a broadband response as shown in Figure 24. The use of narrowband channels simplifies the design of the equalizer, which is necessary to obtain the optimum gain at all frequencies in the cooling band. To design the equalizer, each channel would have its own gain and phase knob.

Just as in the 2-4 GHz design, the pickup arrays will be cooled to  $20^\circ\text{K}$ . The 4-8 GHz slot arrays could be designed to plunge and will probably have a much smaller cross-sectional area than a 2-4 GHz array by about a factor of three. This would allow the vacuum tanks to be smaller and the cryogenics to be more efficient. Also, there would be only one termination per array instead of one termination per loop as in the 2-4 GHz design. This single termination could be placed outside tank. For the kickers, placing the termination outside the vacuum tank would eliminate the need for water cooling inside kicker tank.

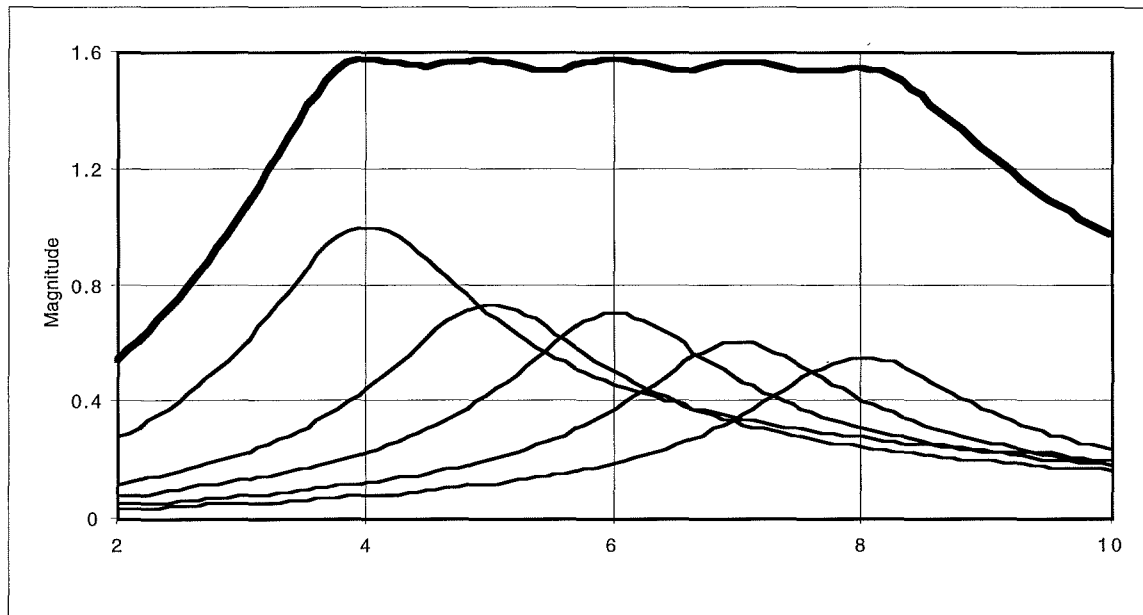


Figure 24. Narrowband arrays are summed to form a broadband response

### 3.9.2 4-8 GHz Signal Transmission

It is impossible to transmit high frequency microwave signals over long distances with single-mode coaxial cable. As the frequency increases, the cable diameter must decrease to avoid dispersion from higher order modes. At 4 GHz the signal loss in crossing the Accumulator ring is about 40 dB. At 8 GHz it is 80 dB. Light can be transmitted long distances with low attenuation, so a laser modulated at microwave frequencies is an attractive choice for transmitting microwave signals. We already have considerable experience in transmitting signal in optical fibers (for use in microwave notch filters). However, the propagation velocity in optical fibers is too slow to transmit signals across a ring; this transmission must be made in vacuum or air. A disadvantage of using the optical technique is the conversion loss in converting the microwave signal to an optical modulation and the consequent reduction in dynamic range.

Development of an optical microwave link that can propagate a signal in the air has progressed to the bench prototype. Procurement of optical telescopes, beam expanders, microposition equipment has been completed. The test setup shown in Figure 25 was mounted on a 3 by 6 foot light table. The network analyzer is used in averaging mode. The system is microphonic with plus minus one dB of vibration jitter. Some of the important parameters are: the DFB laser emits 3.24 mW at 1310 nm, 2.92 mW is transmitted through the second telescope and focused on the second grin lens/beam collimator. Careful tuning was able to couple 2.1 mW of

this optical power into the single mode fiber. A careful optical/microwave calibration was performed on the system. The microwave calibration was taken at 5 GHz with 16 averages and 3% bandwidth smoothing. The dials on the micropositioner are in microns with one full turn of the coarse adjustments equal to 500 microns. The nanotrak system has piezo motion control of 30 microns in  $x$  and  $y$  planes on the micropositioner.

## Optical Transmission Test Setup

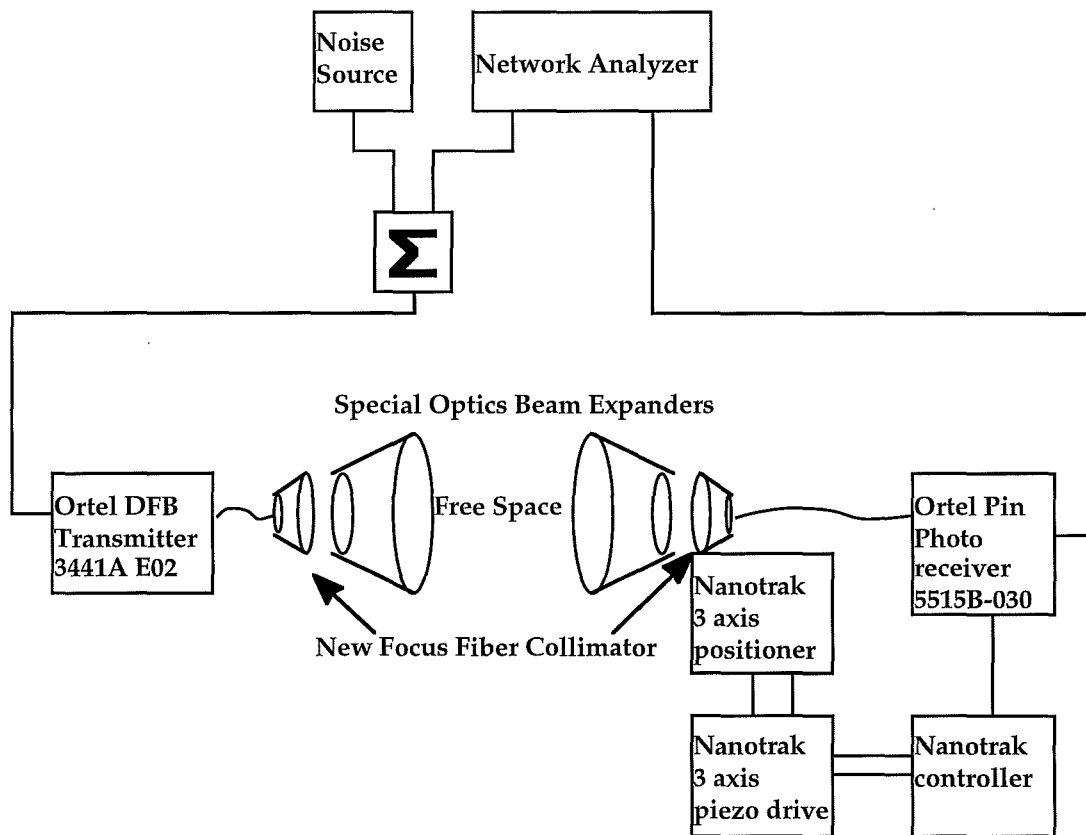


Figure 25. Test set up on 3 x 6 foot light table. Initial results were obtained with 2 inch spacing between beam expanding telescopes.

Some results from this initial test set up are shown below. The transmission (amplitude and phase) across the 0.5-10.5 GHz band are shown in Figure 26. The stability of the optical link is critical to successful performance of the stochastic cooling. The variations in the optical power and microwave signal with respect to perturbations caused by drifts in alignment, temperature, and other time dependent phenomena are being studied in bench tests. A field test of the optical link will occur this year.

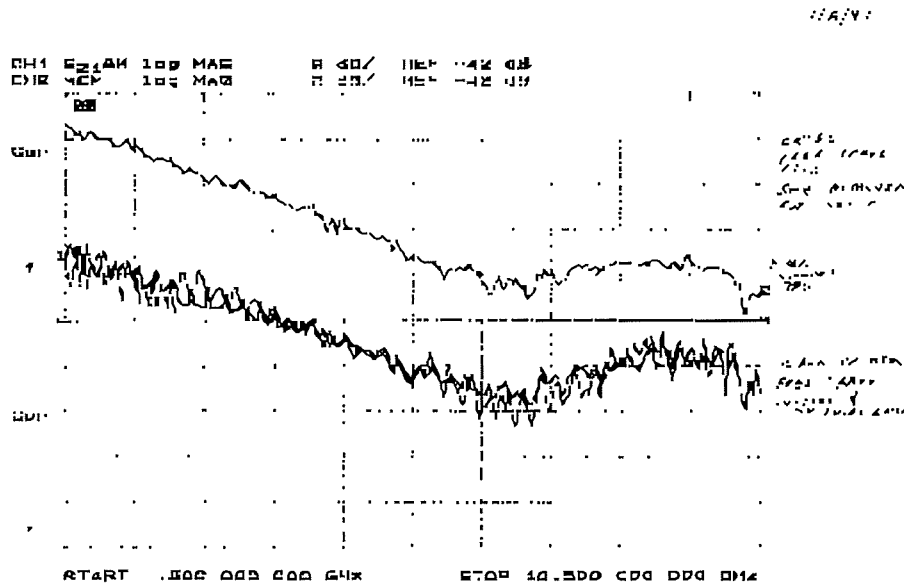


Figure 26. Microwave transmission in the 0.5-10.5 GHz band. Top trace fiber to fiber connect through. Bottom traces free space connect through over a 24 hour period with position tracking. Scale is 2 dB per division.

### 3.10 Antiproton Electron Cooling

Electron cooling of the 8 GeV antiprotons in the Recycler provides an attractive solution to the problem of cooling large stacks of antiprotons. The proposed electron cooling system is similar to the one proposed by IUCF proposal to cool 12 GeV protons in the SSC Medium Energy Booster.<sup>21</sup> Although electron cooling has now become a routine tool in many laboratories, its use has been restricted to lower energy accelerators (<500 MeV/nucleon). An R&D program is currently underway at Fermilab to extend electron cooling technology to the GeV range.

Since the electron energy has to be approximately 4 MeV, the use of traditional electron cooling technology with a Cockcroft-Walton (C-W) power supply and a magnetically-confined electron beam is impractical. In fact, compact commercial C-W voltage generators are limited to about 1 MV, about a factor of 3 times higher than the IUCF, CELSIUS, and GSI electron cooling systems. In the medium energy regime the Pelletron® (Van de Graaff generator type) electrostatic accelerators, having an operating range of about 2-20 MV, would replace the C-W generators. In this regime the continuous longitudinal magnetic field is no longer strictly necessary for focusing although longitudinal focussing still has advantages. The beam focusing requirements are discussed in more detail below.

#### 3.10.1 Electron Cooling Rate

Electron cooling is accomplished by merging an antiproton beam with a co-moving electron beam in a short region of a storage ring. Ions moving in the accompanying electron beam rest frame lose energy by coulomb interactions. The transverse ( $1/\tau_{\perp} = 1/\epsilon_n d\epsilon_n/dt$ ) and longitudinal

®Pelletron is a registered trademark of National Electrostatic Corporation (NEC)

( $1/\tau_{\parallel} = 1/\sigma d\sigma/dt$ ) electron cooling times of an ion beam with transverse normalized emittance  $\epsilon_n$  and relative momentum spread  $\sigma = \Delta p/p$  are well approximated as

$$\tau_{\perp} \approx \frac{A}{Z^2} \frac{\gamma^2}{4\pi\eta\Lambda} \frac{M}{m} \left( \frac{kT_e}{mc^2} \right)^{3/2} \frac{1}{nr_e^2 c} \left[ \sqrt{\frac{8}{\pi}} + u_{\perp}^3 \right], \quad [12]$$

$$\tau_{\parallel} \approx \frac{A}{Z^2} \frac{\gamma^2}{4\pi\eta\Lambda} \frac{M}{m} \left( \frac{kT_e}{mc^2} \right)^{3/2} \frac{u_{\parallel}}{nr_e^2 c} \left[ 1 + u_{\parallel}^2 \right].$$

[13]

Eqn. [12] and Eqn.

[13] include the effects of the “flattened” electron velocity distribution.  $A$  and  $Z$  are the ion atomic number and charge state;  $\gamma$  is the usual relativistic parameter;  $\Lambda$  is the Coulomb logarithm ( $\approx 10$ );  $k$  is the Boltzmann constant;  $m$  and  $M$  are the electron and proton masses;  $c$  is the speed of light;  $n$  is the laboratory frame electron beam density; and  $r_e$  the classical electron radius; all other symbols are defined in Table XIII. The quantities  $u_{\perp}$  and  $u_{\parallel}$  are the nondimensional ion transverse and longitudinal velocities normalized to the electron beam rms transverse velocity:

$$u_{\perp} = \sqrt{\frac{\beta\gamma\epsilon_n mc^2}{\beta_i kT_e}}; \quad u_{\parallel} = \beta \frac{\Delta p}{p} \sqrt{\frac{mc^2}{kT_e}} \quad [14]$$

where  $\beta$  is the usual relativistic parameter and  $\beta_i$  is the ion beta-function in the cooling region. Electron cooling is most effective when  $u \leq 1$ ; in this regime the first addends in the square brackets of Eqn. [12] and Eqn. [13] dominate. Note, that the longitudinal cooling time (2) is roughly proportional to the ion beam momentum spread. This approximation is only valid for “flattened” electron velocity distribution and when the longitudinal ion velocity in the moving frame is greater than the electron beam longitudinal rms velocity spread.

### 3.10.2 Electron Beam Optics

In evaluating Eqn. [12] and Eqn.

[13] we have taken the electron beam temperature to be 0.2 eV. This number is somewhat arbitrary but is defined by the following considerations. Let's assume that a standard tungsten dispenser cathode of 7 mm diameter is used, which gives the intrinsic electron beam temperature at the cathode of 0.11 eV, or 1050 °C. If we now assume that the electron beam is accelerated and expanded to a diameter of 2 cm, the electron beam temperature becomes 13 meV, or 12  $\mu$ rad transverse one-dimensional rms angular spread. However, if there exists a misalignment between the electron and antiproton beam trajectories of this order or greater, or if the electron beam optics is not adjusted so as to make the beam parallel to this order or greater, there will be effective temperatures in excess of the cathode temperature. We feel confident that the two beams can be aligned to better than approximately 40  $\mu$ rad, and that the angular spread due to the electron beam space charge can be kept below this value, thus giving us a conservative estimate for the electron beam temperature of 0.2 eV. This is not a trivial goal when one considers that the earth's magnetic field alone would cause a hundreds of mrad deflection of the electron beam over the 66 m cooling length.

## FIGURE NOT AVAILABLE AT THIS TIME

Figure 27 is an overall view of the proposed electron cooling system in the Recycler.

The electron beam is generated in the 4.3 MV terminal of a Pelletron accelerator. Two solenoids at the beginning of the cooling straight produce the required beam size and convergence. Following the cooling straight section, the beam is then transported back to the 4.3 MV terminal and collected. The simplest electron focusing channel in the cooling region is a series of very weak solenoids with focal length  $f_{sol}$  spaced by the distance  $L_{sol}$ . Figure 28 shows a typical 2-m long module incorporating the electron beam optics, alignment, vacuum, and diagnostics system in the cooling region. Each solenoid in this module provides just enough focusing to locally correct the electron beam expansion due to its space charge. Consequently, this section is optically equivalent to a drift: to first order, a particle entering off axis, but with no transverse momentum, will leave the section with the same transverse position and with no transverse momentum. Assuming that the electron beam current density is uniform one can obtain a simple relation, connecting the solenoid focal length,  $f_{sol}$ , with other parameters:

$$f_{sol} = \frac{r_b^2}{2KL_{sol}}; \quad K = \frac{I_e}{\beta^3 \gamma^3 I_o}, \quad [15]$$

where  $I \approx 17$  kA. Thus, by choosing the 2 m long module, this expression gives the solenoid focal length  $f_{sol} \approx 184$  m and the maximum beam divergence in this case is  $r_b / (2f_{sol}) \approx 27 \mu\text{rad}$ .

Such a seemingly simple focusing system is not without drawbacks, however. For example, if the space charge of the electron beam is compensated by a factor of  $\gamma^2$  ( $\approx 1\%$ ) due to residual gas ions, the electron beam will converge in uncontrollable way (the solenoids can only focus the beam). In addition, this focusing scheme is susceptible to various electron beam instabilities, which might turn out to be detrimental for the high current electron beam transport through the cooling section. One might also argue that in the case of weak periodic focusing the Coulomb logarithm  $\Lambda$  could be a factor of 2 lower than the value used for evaluation of the cooling times in the previous section. This effect is especially obvious for the "slow" (compared to the time-of-flight through the cooling section) collisions between the electron and antiproton. In this regime the electron is "smeared" by the periodic focusing, thus increasing the minimum impact parameter and, consequently, reducing the Coulomb logarithm. This effect is similar to the reduction of  $\Lambda$  for magnetized cooling. All these phenomena as well as alternate focusing schemes (e.g., a solenoidal field) are currently under investigation.

### 3.10.3 Technical Considerations

In addition to the electron beam optics design in the cooling region there are two more principal technical problems which need to be addressed in order to build a 4 MeV electron beam cooling system: (1) the electron beam energy regulation and (2) the efficient and stable recirculation of an electron beam. Below, each of these problems is briefly discussed.

#### 3.10.3.1 Electron beam energy regulation

Pelletrons are commercially available with the short-term stability (ripple) of  $\pm 20$  ppm (parts per million) using a generating voltmeter (GVM) for feedback<sup>22</sup>. This small amount of ripple would have a negligible effect upon the cooling time. Long-term regulation of a Pelletron, however, is substantially worse.<sup>23</sup> Using the standard corona probe feedback system with an error

signal from the GVM, a non-temperature-stabilized Pelletron will drift by as much as 800 ppm/hr, and a thermally-insulated Pelletron by about 75-100 ppm/hr.

Thus, the standard short-term Pelletron regulation should be more than adequate for use in the Recycler. The long-term stability can be greatly enhanced by using an external energy measurement system, for example, a BPM system in a region of high dispersion in the electron beamline.

### 3.10.3.2 High Collection Efficiencies and Stable Recirculation

Achieving stable recirculation of a nonmagnetically confined electron beam is the most significant technical obstacle. Since a Pelletron accelerator will only source on the order of a few hundred  $\mu\text{A}$ , the system must have collection efficiencies of at least 99.99% for operation of a several ampere electron beam. With magnetically-confined beams, such collection efficiencies are easily achieved. In fact, at IUCF, collection efficiencies of 99.9999% have been demonstrated.<sup>24</sup> Our goal is to demonstrate reliable, high efficiency, dc recirculation of a 2 A electron beam using the 2 MV Pelletron accelerator at NEC. Our R&D plan to achieve stable recirculation has been described by Nagaitsev.<sup>25</sup>

Table XIII. Summary of the parameters for the Recycler electron cooling system.

Parameter	Symbol	Value	Units
<b>Recycler Ring Properties</b>			
Circumference	$C$	3319.4	m
Cooling region length	$L_c$	66	m
Fraction ( $L_c/C$ )	$\eta$	0.02	
Cooling region beta-function	$\beta_l$	200	m
<b>Antiproton Beam Properties</b>			
Momentum	$p$	8.9	GeV/c
Transverse emittance (rms, normalized)	$\epsilon_n$		
stacking		1.6	$\pi$ mm mrad
recycling		3.3	$\pi$ mm mrad
Momentum spread (rms)	$\Delta p/p$		
stacking		$2 \times 10^{-4}$	
recycling		$9 \times 10^{-4}$	
Max. antiproton current	$I_p$	200	mA
Laslett tune shift	$\Delta Q_{SQ}$	0.01	
<b>Electron Cooling System Parameters</b>			
Electron current	$I_e$	2	A
Electron kinetic energy	$U$	4.3	MeV
Electron beam radius	$r_b$	1	cm
Electron beam temperature	$kT_e$	0.2	eV
Transverse cooling time (stacking)	$\tau_{\perp}$	90	s
Longitudinal cooling time (stacking)	$\tau_{\parallel}$	20	s



## FIGURE NOT AVAILABLE AT THIS TIME

Figure 27. Electron cooling system layout in the Recycler.

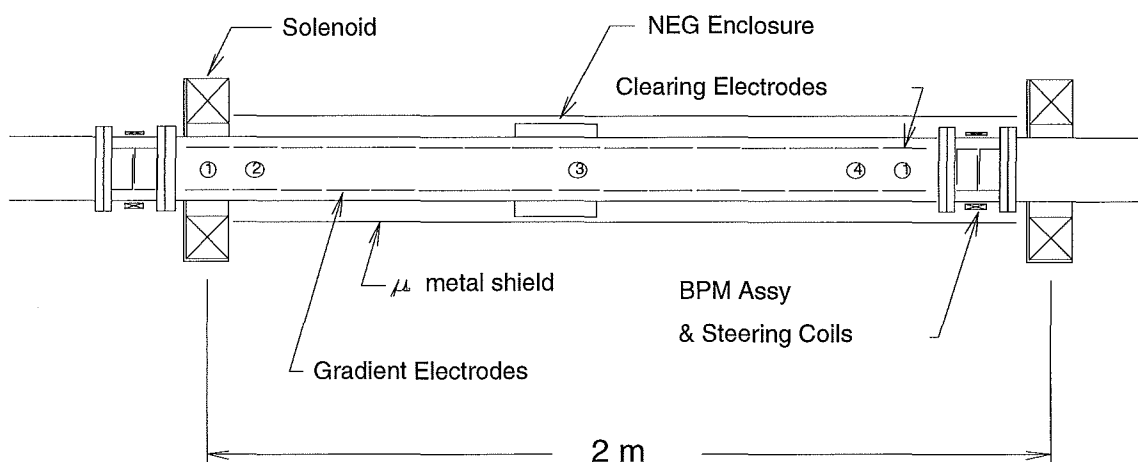


Figure 28. Electron confinement, alignment, vacuum, and clearing system. Every 2 m there is a solenoid, beam position monitor (BPM) and steerer pair, nonevaporable getters (NEG's), and gradient and clearing electrodes.

### 3.10.4 Alternative approaches

Most of the practical work to date has concentrated on the Pelletron approach. However, a parallel effort is considering alternative methods of obtaining the electron beam. We have considered pulsed Linac's with recirculation and betatron accelerators. These devices have potential cost and performance advantages over the Pelletron.

## 4. Colliding beams issues

### 4.1 Tevatron Injection

The bunches in TeV33 will probably be spaced at 7 rf bucket (39.5 m) intervals. The trigger electronics for the two major detectors (CDF and D0) are being upgraded for a 7 rf bucket spacing. Smaller spacing between bunches or even unbunched beams have been discussed but are not considered here. A gap in the beam to accommodate injection and extraction (the beam abort) is required.

At the termination of a normal store, only the protons are removed, and they will probably be removed without the use of the abort kickers. However, we plan to use the abort kickers in abnormal situations to remove the beams quickly without quenching the superconducting magnets. The existing beam abort kickers require a minimum gap of 2.6  $\mu$ sec (139 rf buckets) to rise to a

field which is adequate to steer the beam onto the abort dump. The major experimental areas are located at B0 and D0: 1/3 of the circumference of the ring apart. Loading the ring in a three-fold symmetric fashion provides an identical pattern of interactions at the two interaction regions. Non-symmetric patterns are possible and can have some advantages; a non-symmetric pattern would almost certainly be used if there were only one detector.

The antiproton injection kicker has been built for use in Run II and has a rise time of 400 nsec (21 rf buckets). We plan to modify the proton injection kicker to have a similar rise time. The rise times of the injection kickers requires additional gaps in the bunch trains. The bunch loading scheme used in the present analysis, which satisfies the above constraints, calls for three groups of bunches, each 371 rf buckets long to fill the 1113 Tevatron rf buckets. A group consists of 3 batches of 10 bunches spaced at 7 rf bucket intervals. The batches are separated by 20 rf buckets for the injection kicker and the last batch is followed by the abort gap of 139 empty rf buckets. This scheme is illustrated in Figure 29

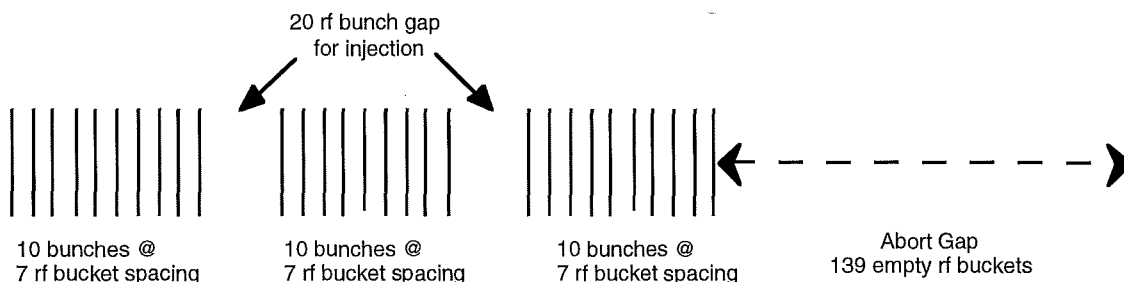


Figure 29. Nominal bunch structure for TeV33.

The gaps in the beam cause an undersirable spread in the beam-beam tune shift parameters. With the scheme illustrated in Figure 29, only 90 out of 159 potential rf buckets are filled. If some of the gaps were eliminated or reduced, and the total number of antiprotons were held constant, the number of interactions per beam crossing could be reduced. We expect that the actual configuration of bunches will change as we study the beam-beam interaction and the beam loading constraints in more detail.

## 4.2 Proton Intensity

The TeV33 proton intensities are specified to be the same as those used in Run II and, in fact, already achieved in the Main Ring. Simulations predict that 5 bunches, each with  $6 \times 10^{10}$  particles in a longitudinal emittance of 0.15 eV-sec can be coalesced into a single 1.38 eV-sec bunch with  $27 \times 10^{10}$  particles.<sup>26</sup>

A simulation for seven bucket spacing has also been performed. In order to achieve good coalescing efficiency with 5 bunches, the rf waveform must be linearized using higher harmonics of the rf. The simulation used first, second, and third harmonics of the basic 7.58 MHz frequency (7 bucket spacing). The results of the simulation are shown in Figure 30. Each of these frequencies would be created by a new, albeit, modest rf system. The new rf systems are summarized in Table XIV.

Based on beam experiments with multi-bunch coalescing, we know that beam loading effects are important. The simulation has not taken these effects into account. Some of the measures we plan to use to reduce beam-loading effects are discussed in section 3.1.3.3. The number of bunches that can be simultaneously coalesced will affect the loading scheme. At the moment, we plan to simultaneously coalesce 12 bunches.

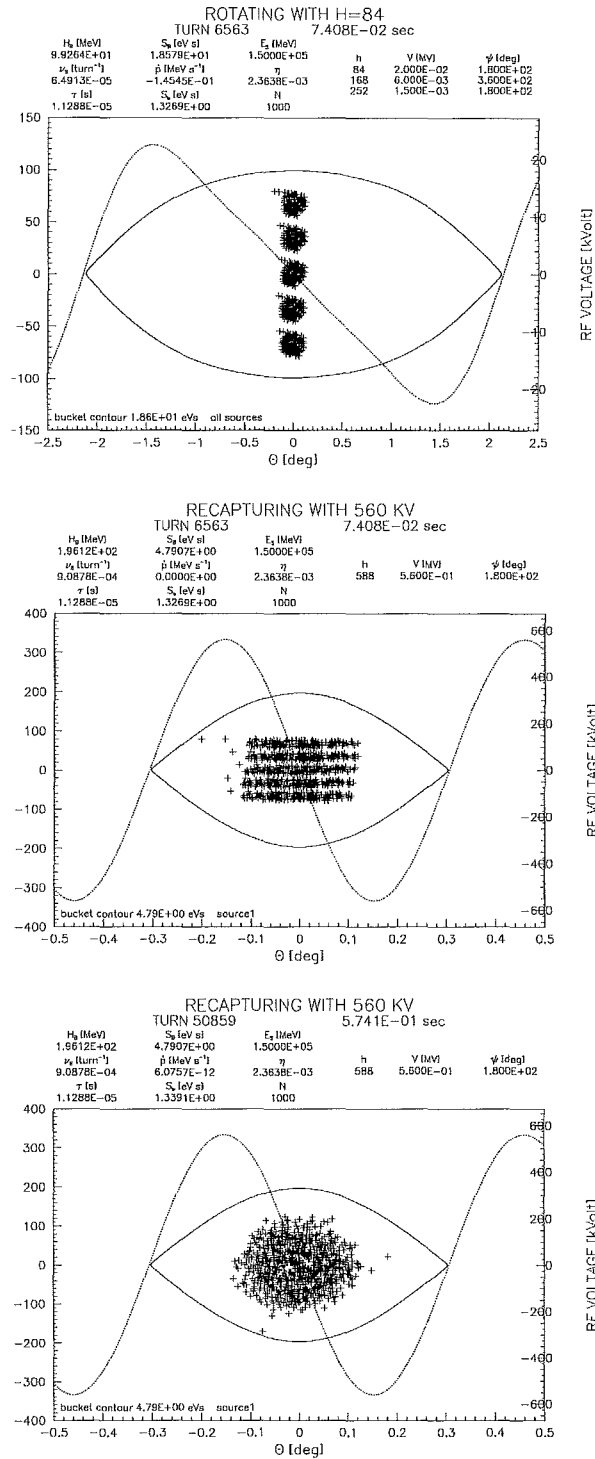


Figure 30. A simulation of the proton coalescing process. The beam distribution and rf wave form is shown (a) after rotation with the (linearized)  $h=84$  rf, (b) immediately after recapture with the  $h=588$  (53 MHz) rf, and (c) as the beam approaches its equilibrium distribution in the  $h=588$  bucket.

Table XIV. New rf systems required for proton coalescing in the Main Injector

Harmonic	Frequency (MHz)	Voltage (kV)
84	7.59	20
168	15.17	6
252	22.76	1.5

### 4.3 Antiproton Intensity

The same coalescing hardware could be used to form the antiproton bunches, but it is likely to unnecessary. The Main Injector is expected to be capable of acceleration 0.5 eV-sec bunches through transition. The total Recycler longitudinal beam emittance will be 20 eV-sec or less (see Table xxx). The Recycler beam could thus be packaged into batches of 12 bunches with 7 bucket spacing, each bunch having an emittance of  $20/100=0.2$  eV-sec. These bunch trains could be accelerated directly by the Main Injector.

Thus, the Recycler has the potential to deliver antiproton beams with longitudinal emittances well below the 2 eV-sec listed in Table II. Such low emittance bunches could produce large tune shifts in the proton beam, be subject to rapid growth from intrabeam scattering, and be subject to instabilities (such as the fast head-tail mode). We may choose to dilute the beam to the 2 eV-sec emittance listed in Table II in order to avoid some of these effects, or we may chose to take advantage of the increased luminosity available from lower emittance beams. If we should find it necessary to blow up the emittance before transition in the Main Injector, we would use the coalescing technique described in section 4.1 for the protons also.

### 4.4 Tevatron rf voltage considerations

One of the more important factors in the luminosity form-factor ( $F$  in Eqn. [1]) is the bunch length. The bunch length is determined by the rf Voltage and the bunch emittance. For gaussian beams in a stationary bucket having emittances small compared to the bunch area:

$$\sigma_1 = \sqrt{\frac{\eta \epsilon_L^2}{18\pi(ehV)E_0\omega_0^2}} \quad [16]$$

As shown in Table II, the existing 1 MV of rf at 53 MHz results in an rms bunch length of about 36 cm. This can be reduced to 13 cm with a 16 MV system operating at 212 MHz. Figure 31 shows a comparison of the average integrated luminosity that could be obtained with and without the rf upgrade<sup>27</sup>.

The evolution of the beam emittances during a store is expected to be dominated by intrabeam scattering and should be rather different in the cases with and without the rf upgrade. The evolution of longitudinal and transverse emittances are shown in Figure 32 and Figure 33.

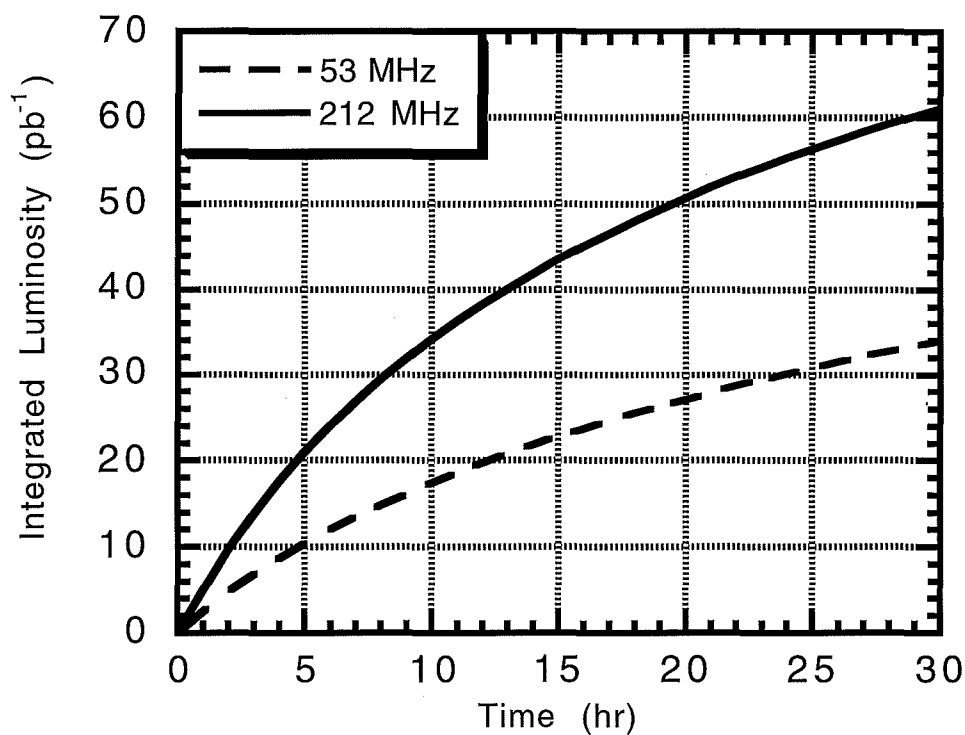


Figure 31. The average store luminosity as a function of time between stores. The average luminosity increases with store length because there is more time to accumulate antiprotons and the initial antiproton intensity is higher.

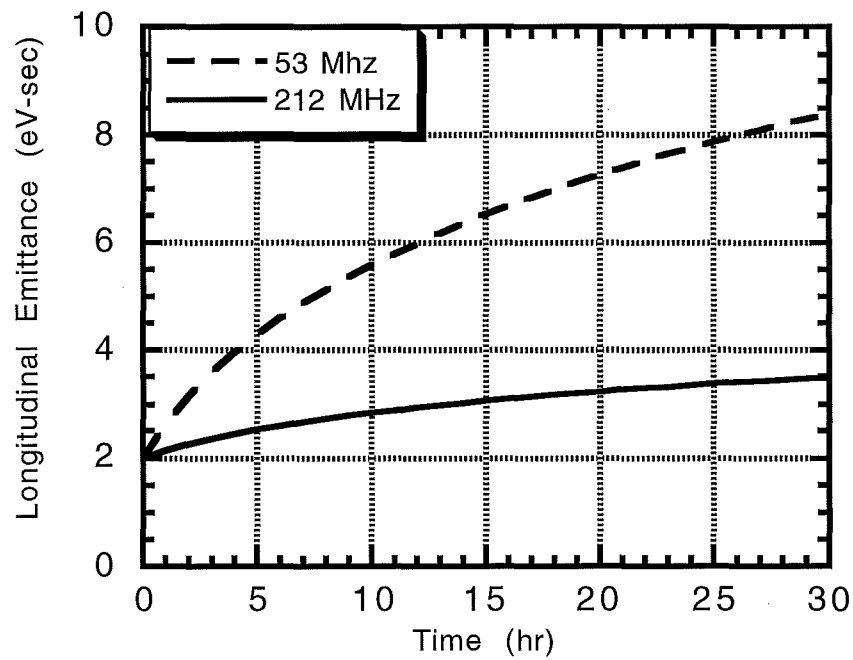


Figure 32. The longitudinal emittance as a function of time into the store. The larger momentum spread obtained with the higher voltage, 212 MHz rf system dramatically reduces the longitudinal growth.

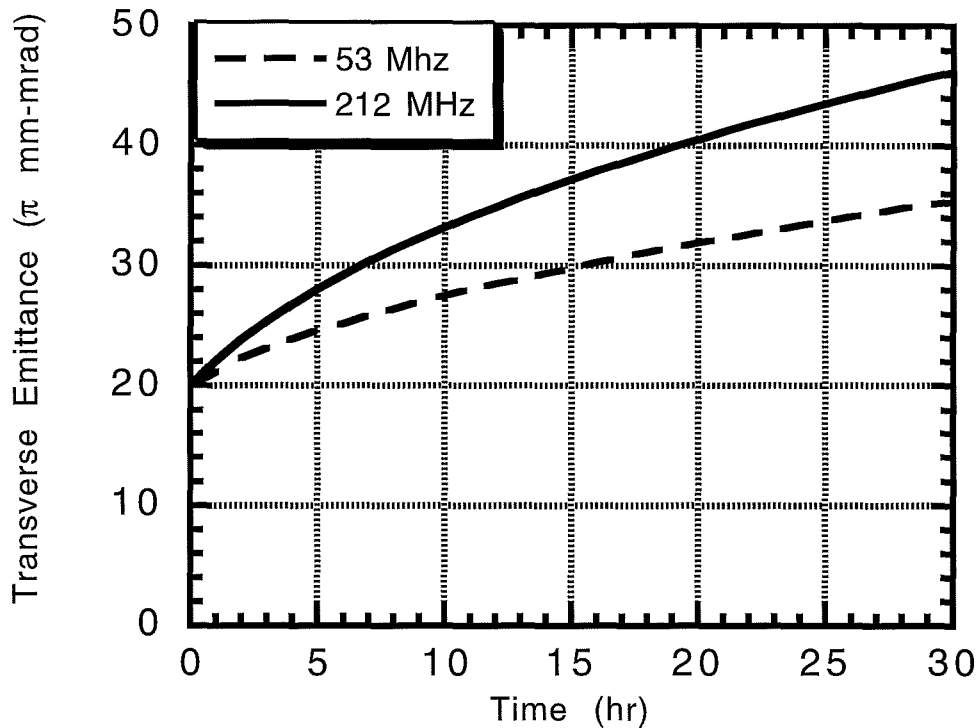


Figure 33. The transverse emittance as a function of time into the store. The shorter bunch length obtained with the 212 MHz rf system increases the transverse beam growth.

Stronger rf focusing could be obtained with either conventional or superconducting technology. Since no power is delivered to the beam when the beams are stored, superconducting technology is a natural choice. With an inductively tuned superconducting cavity, the beam current will excite the cavity, producing the necessary voltage. While this approach appears promising, it will be necessary to establish the techniques required to capture the beam into the desired buckets and to examine the beam stability. We have postponed a more detailed look at these beam dynamics issues because the rf upgrade, if feasible, will be an expensive proposition and will occur, if at all, in the later stages of the TeV33 upgrade.

#### 4.5 Single beam stability

Beam instabilities can be divided into two types: single-bunch and multi-bunch instabilities. The single-bunch may be caused when a bunch's wake fields act on itself. Multi-bunch instabilities may be caused when the wakefield acts on subsequent bunches. The proposed single bunch intensities for TeV33 are essentially the same as those already achieved. Therefore, the instabilities expected are those known from current operation. A head-tail transverse instability is observed<sup>28</sup> when the chromaticity is negative. In normal operation, the chromaticity is maintained at about  $\xi=+10$  to provide a margin against this instability. When the beams are colliding, where the instability is presumably stabilized by the tune spread from the beam-beam

tune shift, the chromaticity is reduced towards zero. The long range beam-beam tune shift in TeV33 results in a spread in bunch-by-bunch chromaticities, so we plan to suppress the instability with the new Tevatron bunch-by-bunch damper. The damper may cause excessive emittance growth if used for more than a few minutes, but we expect beams should be stable when collisions are achieved.

We have also observed what appears to be a longitudinal head-tail instability.<sup>29</sup> This instability is suppressed by a longitudinal bunch-by-bunch damper designed for 6 bunch operation.<sup>30</sup> This damper system will need to be upgraded by handle 36 bunches in Run II and ultimately 159 bunches for TeV33.

Multibunch instability thresholds depend primarily on the total current. TeV33 will be significantly more susceptible to multi-bunch instabilities the case in Run I (6 bunch operation). However, based on fixed target operation (with  $2.5 \times 10^{13}$  particles), we expect transverse instabilities from the resistive wall effect and longitudinal coupled bunch instabilities from the cavity modes. The resistive wall instability is not seen in the Tevatron when the chromaticity is tuned to be positive. The most severe longitudinal coupled bunch instability appears to be a mode-1 instability. Since neither of these instabilities is particularly vicious in fixed target operation, we expect to be able to control them in Collider operation.

#### 4.6 Beam abort

The role of the Tevatron abort will change dramatically when antiproton recycling becomes a reality. The existing A0 abort removes protons and antiprotons from the accelerator simultaneously in a single turn and consequently be used if the antiprotons are to be retained at the end of the store. The role of the A0 abort in Run II and beyond would be to:

- 1) Provide a beam dump when proton-only stores are used (including the normal tune-up of beam transfers.
- 2) Remove colliding beams urgently—to avoid a quench, for example.

The effectiveness of the abort for colliding beams is limited by the following factors:

- 1) It is difficult to develop a signal that reliably indicates the need for an urgent abort. For example, the loss monitor system that is used in fixed target operation is not allowed to trigger the abort in colliding beams operation.
- 2) Some faults (such as a refrigeration failure) typically result in quenches whether or not the beam is removed.
- 3) There are times during the injection process and possibly during acceleration when the beams are not appropriately clogged to make possible an abort without excessive (quench inducing) losses.

Despite the limited use of the A0 abort, we tentatively plan to retain it in its current configuration and to use it whenever possible to minimize the number and the severity of quenches and to provide a more controlled removal of the beam energy and better confinement of the resulting radioactivity.

The intensity limitations<sup>31</sup> of the A0 abort are summarized in Table XV. The yearly dose rates assume a utilization of 7200 proton beam aborts at 150 GeV, 6 proton beam aborts at 1 TeV, and 2 antiproton beam aborts per day for 183 days per year. The most serious limitations are the activation of the absorber and soil contamination. The soil contamination problem can be mitigated by the addition of steel on the outside of the existing absorber. The 0.1 Rad/hr limit on the residual activity is somewhat arbitrary but could probably be reached by adding some additional shielding to the existing absorber.



**Table XV. Intensity limits of the A0 abort**

Subject	Limiting Parameter	Max Beam Intensity
Beam loss (quench)	<0.1 mJoule/gm	$2.6 \times 10^{14}$
Residual Radioactivity	<0.1 Rad/hr @ 24 hrs	$4.4 \times 10^{12}$ @ 150 GeV $2.6 \times 10^{12}$ @ 1 TeV
Energy Deposit. in Graphite	3 KJoule/gm	$4.5 \times 10^{13}$ @ 1 TeV
Hadrons in Soil	<1.5 E16/yr @ 1 TeV	$2.2 \times 10^{12}$ @ 150 GeV $1.3 \times 10^{12}$ @ 1 TeV
Thermal Power (average)		Not a problem
Muons flux		Not a problem

## 4.7 Interaction Regions

*This section is closely tied to the beam-beam section. It will be revised when the beam-beam section is done.*

It has not yet been decided how many interaction regions will be occupied by experiments during the TeV33 era. One or both of the major interaction regions at B0 and D0 might be occupied. A proposed, new interaction region at C0 might also be occupied. We have not considered in any detail at all, any option other the current operating condition of having high luminosity experiments at B0 and D0.

The low beta insertion at C0, if any, has not been designed (although there has been a significant effort towards this end). The low beta insertions at B0 and D0 are likely to undergo some modification probably at the time of Run II. These modifications, which are described below, have been used in the calculation of the beam-beam effects.

An alternative match to the lattice which gives both  $\eta$  and  $\eta' \equiv 0$  throughout the straight section has been described<sup>32</sup> which uses the current IR physical configuration of magnets and gradients compatible with the existing quadrupoles. Implementation of this design would only require the interchange of two power supplies and a reversing switch. For  $\beta^* = 0.35\text{m}$ , the IR lattice functions and corresponding quad gradients for this dispersion-free solution are shown in Figure 34 and Table XVI.

$$\beta^* = 0.35\text{m}; \beta_{\text{max}} = 1254\text{m}; Q_{x,y} = .585, .575$$

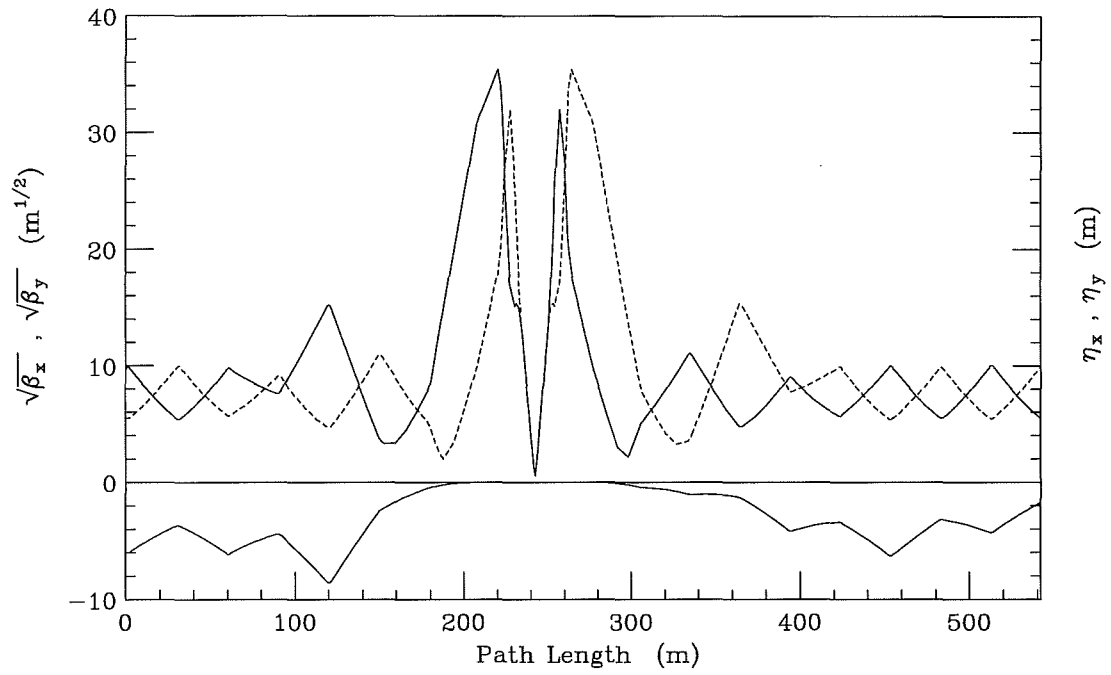


Figure 34. Dispersion-free IR lattice functions for  $\beta^* = 0.35\text{m}$ .

Table XVI. IR quad gradients without separated beams or beam-beam interactions.

Quad #	$\beta^* = 0.35$ m	
	up	down
Q4	120.0349	-120.0349
Q3	-123.9186	123.9186
Q2	120.0349	-120.0349
Q1	31.2039	-31.2039
Q5	-133.0558	133.0558
Q6	-26.6276	26.6276
T6	-1.96143	
T7	33.2027	-32.5509
T9	-46.4417	48.3786
T0	9.08524	-10.7146

Implementation of the zero-dispersion IR configuration would reduce beam-size in the low-beta quads. The horizontal beam size with dispersion is given by the rms spread of the Gaussian distribution:

$$\sigma_x^2 = \frac{\beta_x \epsilon_N}{6\pi\beta\gamma} + \left( \frac{\eta \sigma_p}{p_0} \right)^2 \quad [17]$$

where  $\epsilon_N$  is the (95%) normalized emittance,  $\eta$  is the horizontal dispersion,  $\sigma_p/p_0$  is the momentum spread, and  $\beta\gamma \approx 959$  at 900 GeV/c. For a  $\beta^*$  of 0.35m, in the current Tevatron IR configuration  $\beta_{\max} \approx 1125$ m and  $\eta \equiv 4.6$ m, compared to  $\beta_{\max} = 1254$ m and  $\eta \equiv 0$ m in the zero-dispersion configuration. For  $\epsilon_N = 18\pi$  mm-mr beams and  $\sigma_p/p_0 = 0.5 \times 10^{-3}$ , the dispersionless solution would reduce  $\sigma_{\max}$  from  $\approx 3$  mm to  $\approx 2$  mm, thereby allowing the beams to travel more closely to beamline center and minimize the adverse effects on dynamic aperture.

The crossing angles and separator settings employed in the following tune shift and orbit distortion studies correspond to the IR configuration discussed above. Specifically, for  $\beta^* = 0.35$ m,  $3\sigma$  and  $5\sigma$  center-to-center beam separation at the first crossing are studied for  $18\pi$  colliding beams. The half-crossing angle  $\alpha$  that produces  $n\sigma$  beam separation at the first parasitic crossing is approximately:

$$\alpha \approx \frac{n}{2} \cdot \sqrt{\frac{\epsilon_N}{6\beta^*\beta\gamma}} \quad [18]$$

For  $3\sigma$  and  $5\sigma$  separations  $\alpha$  becomes approximately 142 and 236  $\mu\text{rad}$ , respectively. The separator gradients chosen to create these two cases are listed in Tables III.ii and III.iii., and the corresponding beam separations around the ring are illustrated in Figures III.ii and III.ii. These results are calculated without beam-beam interactions. With interactions bunch-by-bunch closed orbit distortions are introduced, requiring the gradients to be re-adjusted to remove the average distortion of the bunch train.

With these gradients the crossing angle gets divided equally between the horizontal and vertical planes at each IP. This choice is certainly not unique, and extensive additional study is required to determine the optimum configuration.

Table XVII. Separator gradients for  $3\sigma$  separation and 141  $\mu\text{rad}$  half-crossing angle (100  $\mu\text{rad}$  in each plane), calculated without beam-beam interactions. The average beam separation around the ring is  $12.2\sigma$  and a maximum of  $17.2\sigma$ .

Location	Horizontal Separators		Vertical Separators	
	# of modules	gradient (kV/cm)	# of modules	gradient (kV/cm)
A17			1	-23.27275
A49	1	-38.37601	2	44.24674
B11	2	-40.00000	1	-40.00000
B17	4	12.67017		
C17			4	30.81782
C49	1	-28.51545	2	-38.29951
D11	2	40.00000	1	-40.00000
F17	1	-21.01801		

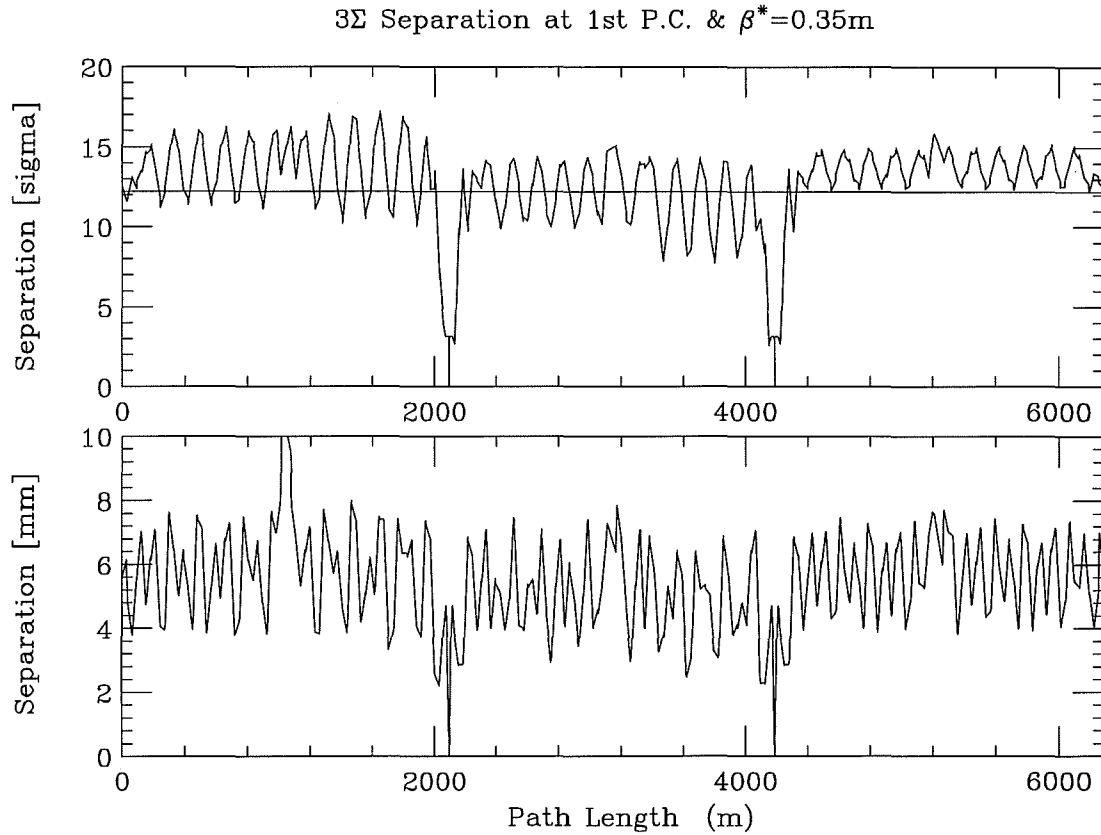


Figure 35. Beam-beam separation around the ring corresponding to  $3\sigma$  separation at the first parasitic crossing.

Table XVIII. Separator gradients for  $5\sigma$  separation and  $240\text{ }\mu\text{rad}$  half-crossing angle ( $170\text{ }\mu\text{rad}$  in each plane), calculated without beam-beam interactions. The average beam separation around the ring is  $13.0\sigma$  and a maximum of  $18.0\sigma$ .

Location	Horizontal Separators		Vertical Separators	
	# of modules	gradient (kV/cm)	# of modules	gradient (kV/cm)
A17			1	-65.19102
A49	1	-37.70542	2	47.59569
B11	2	-40.00000	1	-40.00000
B17	4	4.41813		
C17			4	29.56344
C49	1	-34.47286	2	-35.03936
D11	2	40.00000	1	-40.00000
F17	1	-20.82630		

Table III.iii.

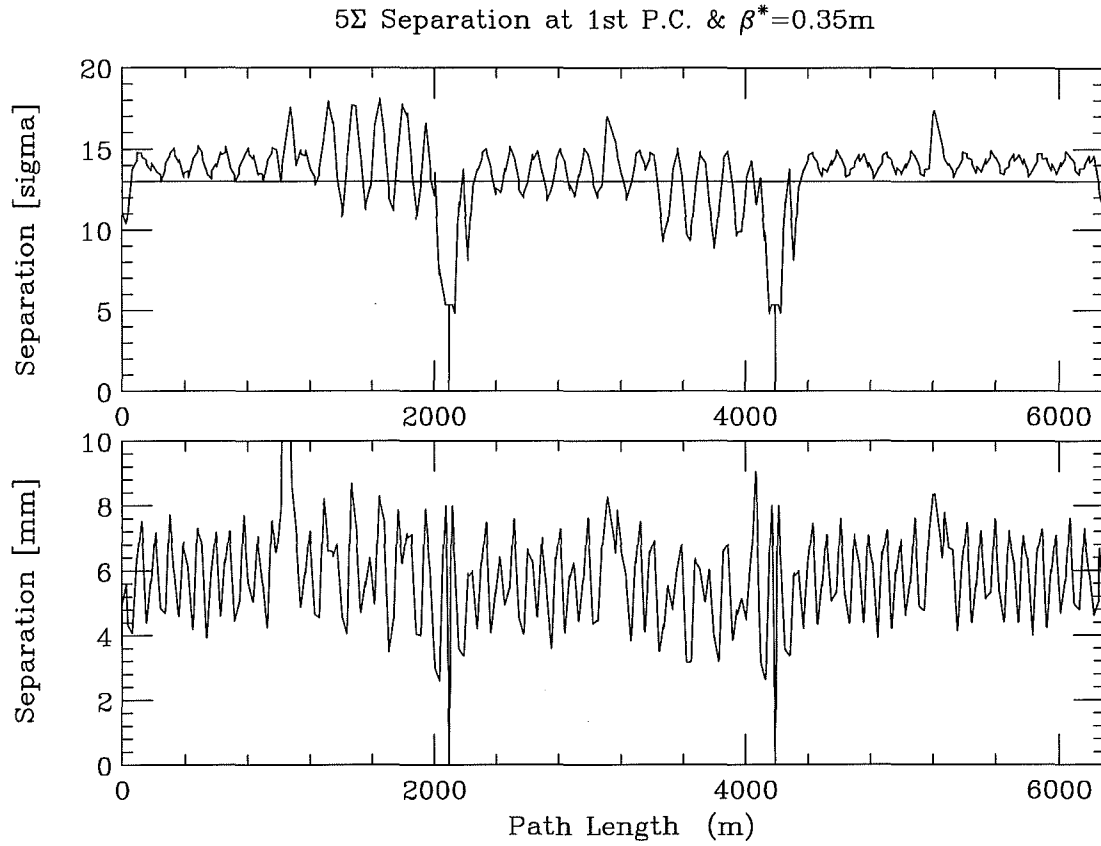


Figure 36. Beam-beam separation around the ring corresponding to  $5\sigma$  separation at the first parasitic crossing.

The  $z$  distribution at the colliding beam can be calculated easily once the bunch length and the crossing angle are known. Figure 37 shows the distribution of vertices for 170 urad crossing angle assuming various bunch lengths.

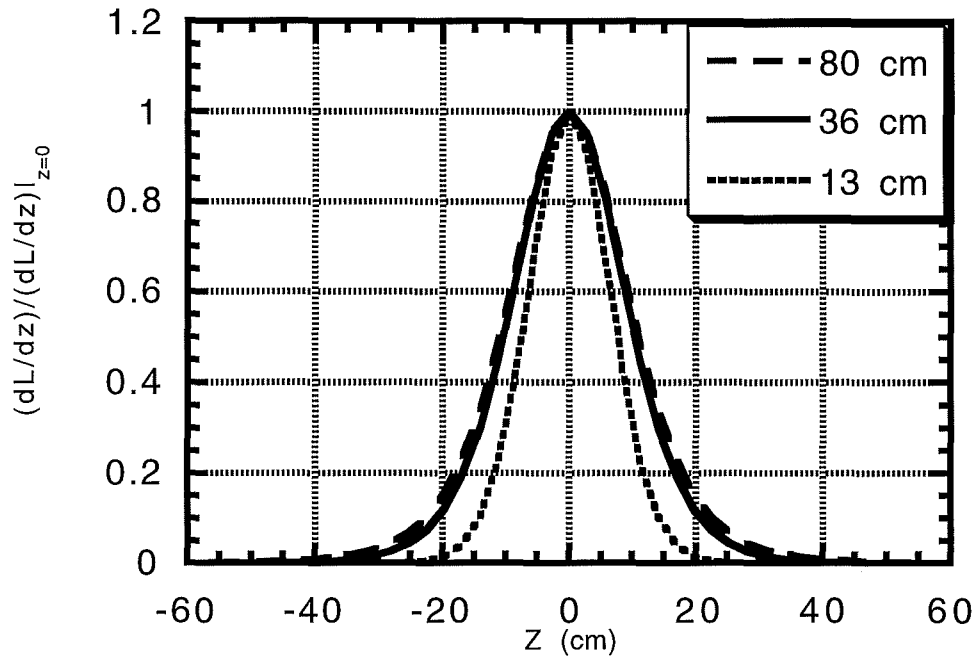


Figure 37. The calculated  $z$  distribution of vertices 170 mrad crossing angle and various bunch lengths. For bunch lengths of 35 cm or more, the distribution is largely determined by the size of the crossing angle.

#### 4.8 Beam-beam effects

*Peter Bagley is working on section 4.8. He is not responsible (very much) for the text below, which is obtained from previous papers via cut and paste. Read it if you like, but it is not guaranteed to be relevant in the current context.*

The beam-beam interaction is the pre-eminent issue in the Tevatron. As the luminosity in the Tevatron rises the number of bunches is increased. The increase has been driven by the desire to keep the number of interactions per crossing low (low means about 10 for TeV33)—although ultimately one would need to increase the number of bunches to keep the antiproton  $N_{\bar{p}}/\epsilon_{\bar{p}}$  less than or equal to that of the protons. While the number of interaction regions remains at 2 (or is possibly reduced to 1), the number of beam crossing points with long-range beam-beam interactions increases with the number of bunches (it is equal to twice the number of bunches minus the number of interaction points). In Run I the antiproton bunches were subjected to 10 long range interactions on every circuit of the Tevatron. In Run II the number will increase to 70 although we have discussed running with 30×36 (antiprotons × protons) to avoid the very different tune shifts experienced by the first and last antiproton bunches.

The current plan for TeV33 is to introduce a crossing angle of about 100  $\mu$ rad to minimize the effects of the parasitic crossings near the interaction region. We will try to optimize the value of the crossing angle based on the considerations mentioned below.

- 1) The beam-beam interaction distorts the closed orbit (up to 20 mm at low beta compared to a nominal beam size of 35 mm) and causes each bunch to have its own unique orbit.
- 2) The beam-beam interaction gives each bunch a unique tune: the spread in these tune shifts is about 0.01 (compared to a total tune footprint budget of 0.025). Similar results are obtained for the coupling. Chromaticities are also different for each bunch.
- 3) The separation at the beam crossing nearest the interaction point is determined by the crossing angle, but subsequent crossings depend also on the separator settings. The signs and strengths of the crossing angle and the separators need to be chosen to optimize the beam separation.

The results of the preliminary beam-beam calculations made to date are not sufficiently encouraging to declare success, nor are they sufficiently disturbing to terminate the plans for TeV33. The beam-beam tune shift is sensitive to many details including the size of the crossing angle and the bunch loading scheme. Much more work will be required to quantify these issues and to achieve a more attractive solution.

The crossing angle causes a reduction in the luminosity and introduces the possibility of exciting synchro-betatron resonances. These effects increase with the size of the crossing angle. The effects of the crossing angle are reduced by making the bunch length shorter. A significant Tevatron rf upgrade is the most likely candidate for reducing the bunch length. We will examine the need for an rf upgrade as a function of crossing angle.



## Crossing Angle Effects

On the Luminosity and the Beam-Beam Tune Shift

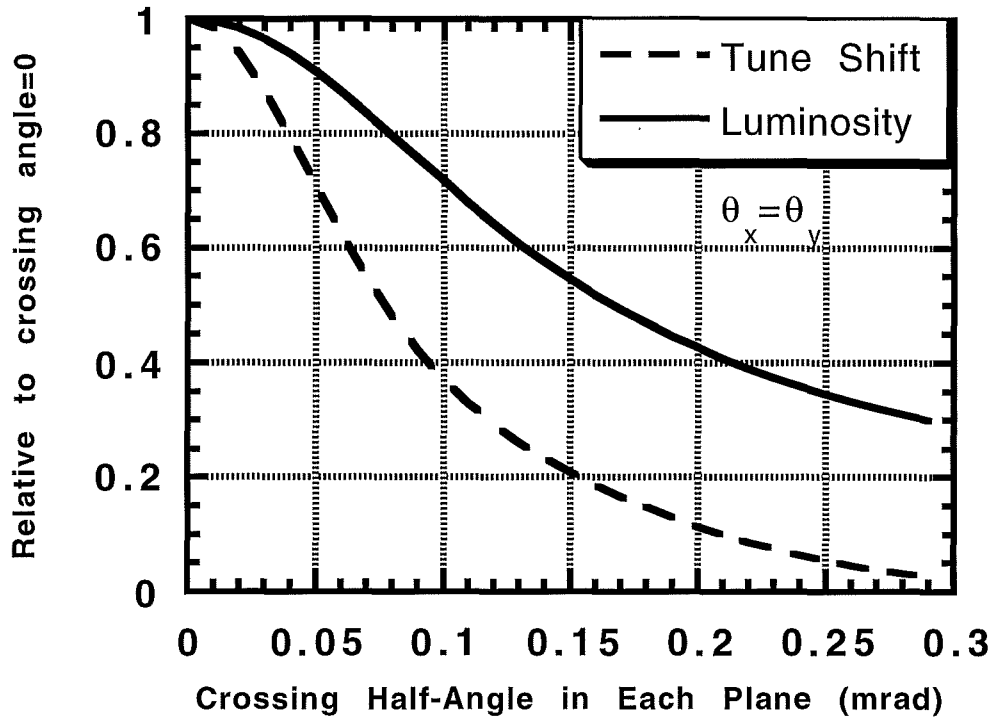


Figure 38. Relative luminosity and tune shift versus crossing angle.

### 4.8.1 Tune footprint

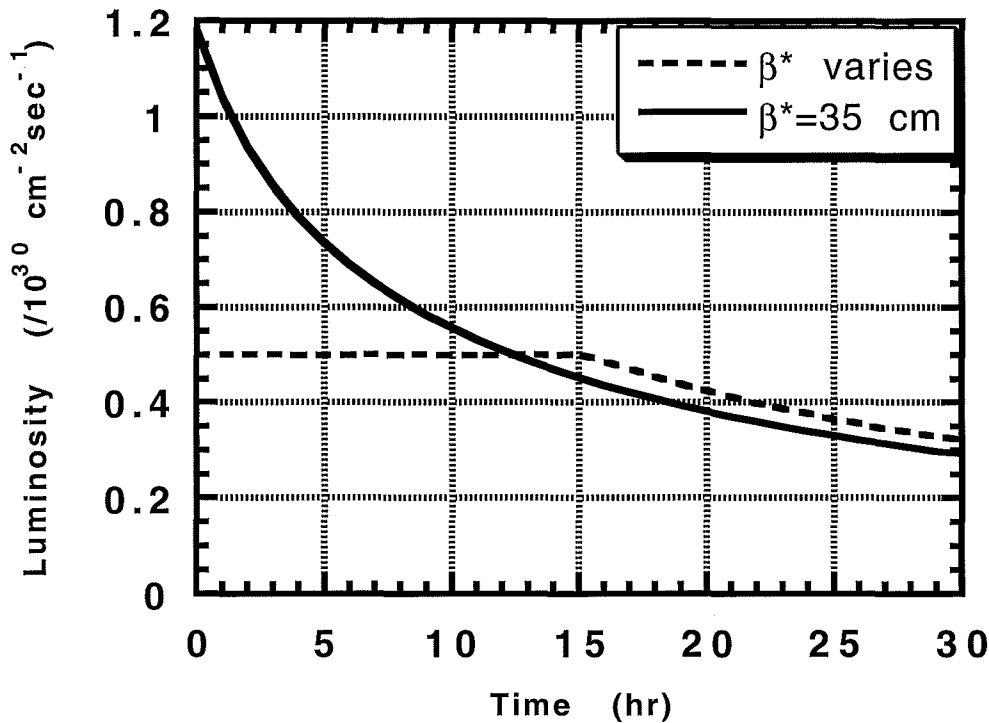
### 4.8.2 Crossing angle

## 4.9 Luminosity Leveling

The peak luminosity of  $10^{33} \text{ cm}^{-2}\text{sec}^{-1}$  with 100 bunches per beam results in about 10 interactions per bunch crossing. It is difficult (and expensive) to build high performance detectors to operate in this environment. One possible operational scenario involves a technique known as "luminosity leveling". The idea is that the luminosity is held at a maximum value—say  $0.5 \times 10^{33} \text{ cm}^{-2}\text{sec}^{-1}$ —during the initial part of the store and kept constant for as long as possible. The luminosity modulation could be accomplished, in principle, by varying any of the beam parameters on which the luminosity depends such as crossing-angle, bunch length,  $\beta^*$ , beam separation, etc. A simulation of luminosity leveling is shown in Figure 39 for the nominal parameters in Table II. The loss of luminosity from intrabeam scattering and residual gas effects is the same for both stores, but the luminosity limited store retains more antiprotons (fewer collisions) and has a higher luminosity at long times in the store.

The limited store yields  $23.4 \text{ pb}^{-1}$  in 14.0 hours (a 13 hour store plus one hour for shot setup) for an average luminosity of  $1.67 \text{ pb}^{-1}/\text{hr}$  compared to  $36.2 \text{ pb}^{-1}$  in 15.6 hr and an average luminosity of  $2.32 \text{ pb}^{-1}/\text{hr}$  for the unlimited store. The average luminosity obtained with a luminosity leveled store is less sensitive to the initial antiproton bunch intensity than a unleveled store, but the highest integrated luminosity is obtained in either case with the highest possible initial antiproton intensity. The loss of luminosity from leveling depends on the store parameters: the importance of the antiproton intensity to the lifetime, the amount of luminosity reduction desired, and the length of the store.

Figure 39. A store with the nominal parameters and  $N_{\bar{p}} = 27 \times 10^{10}$  is compared to an otherwise identical store where  $\beta^*$  is varied to maintain a constant luminosity of  $0.5 \times 10^{33} \text{ cm}^{-2}\text{sec}^{-1}$  for as long as possible keeping  $\beta^* > 35 \text{ cm}$ .



It should not be supposed that luminosity leveling is trivial or even straight-forward. An enormous amount of effort is invested in minimizing beam loss by adjusting orbits, tunes, and chromaticity when the beams collide. The techniques that are used to modulate the luminosity may have adverse effects on the loss rate. One leading candidate to implement luminosity leveling is to modulate the beta function at the interaction point. Our experience is that changes to magnet excitation are likely to result in increased loss rates. It is not clear how well we will be able to control the beam loss rates when changes are made to the machine parameters to keep the luminosity constant.

## 5. Summary of upgrades required.

The following tables are intended to provide a convenient summary the major technical efforts necessary to implement the TeV33 scenario as outlined above. Table XIX summarizes the R&D efforts required. All of these R&D projects represent an extrapolation of existing techniques; they are not design efforts utilizing proven technology. If the R&D should prove to be unsuccessful an alternative technology would have to be identified. Possible alternatives are discussed in section 6.

Table XIX. Table Summary of R&D projects required for Run III

R&D Project	Status
Electron Cooling	underway
4-8 GHz Pickup Design	underway
4-8 GHz Signal Transmission	underway
8-16 GHz cooling technology	deferred
Superconducting rf	deferred
Tevatron Kicker Bump Magnet	underway
Liquid (?) high gradient lithium lens	not started
Pbar aperture definition	not started

Table XX. Summary of upgrades required for Run II and Run II

Construction Project	Funding
Kicker Bump Magnet*	Operating??
Debuncher Cooling Improvements**	AIP96
Accumulator Lattice Change*	AIP97
Pbar Target Sweeping *	AIP98
2-4 GHz Accumulator stack tail upgrade*	AIP98
Tevatron Short Batch Kicker*	AIP99
Booster Extraction (Kickers)	AIP99
Lithium lens	??
QPM Upgrade	AIP99
Pbar Kicker and Septa Improvements	AIP99
Tevatron Correction Package Upgrade	AIP99
TeV BPM Upgrade	AIP00
Main Injector gammat-jump	AIP00
Pbar BPM's Debuncher	AIP01
Main Injector Coalescing rf	Operating??
Improved low level agility (Slip stacking)	Operating??
Beam loading compensation (Slip stacking)	Operating??
pbar aperture upgrade	??
Fiber optic links for 4-8 GHz	AIP??
4-8 GHz Debuncher transverse cooling	AIP??
4-8 GHz Debuncher longitudinal cooling	Unknown
4-8 GHz Accumulator stack tail upgrade	AIP??
Electron cooling	AIP??
Superconducting RF	AIP??

\*Run II upgrades

\*\*The Debuncher Cooling Improvements will use 4-8 GHz technology if the on-going R&D is successful in time to be implemented for Run II. Even if this effort is successful, further upgrades will be necessary for Run III; these are called listed as the "4-8 GHz Debuncher" cooling upgrades.

## 6. Risks & Alternative approaches

### 6.1 Strip-line kicker

### 6.2 Full MI targeting

### 6.3 Risks

#### Electron Cooling

There are other ideas for increasing the number of protons targeted. Some of these are:

- 1) Increasing the Linac Energy
- 2) Replace the existing Booster with a "Super-Booster"
- 3) Betatron stacking in the Main Injector using the existing Booster.
- 4) Targeting the full Main Injector Ring (ref to TM).

These ideas have merit and may be pursued more vigorously in the future.

Linear Debuncher.

## 7. Conclusion

An upgrade in the luminosity of the Tevatron proton-antiproton collider to the vicinity of  $L=10^{33} \text{ cm}^{-2}\text{sec}^{-1}$  appears to be feasible provided that the technological advances described in this report can be realized. A necessary, but not sufficient, condition for the increase in luminosity is a substantial increase in the antiproton accumulation rate. We have proposed a plan to increase the stacking rate by a factor of 4. Another necessary condition is a large increase in the number of bunches colliding in the Tevatron. Our ability to avoid adverse effects from the beam-beam interaction is a primary concern, and an area that is actively being studied. However, based on the beam-beam footprints that have been obtained, colliding large numbers of bunches appears to be feasible.

## References

- <sup>1</sup> TheTeV2000 committee report (unpublished), but currently available on the World Wide Web site <http://www-theory.fnal.gov/tev33.ps>.
- <sup>2</sup> The Fermilab Main Injector Technical Design Handbook, unpublished, but the most recent version is available on the world-wide-web at \*\*\*\*.
- <sup>3</sup> Recycler design book, unpublished.
- <sup>4</sup> D. Herrup and D. McGinnis, private communication. There is a better reference, I think.
- <sup>5</sup> D. Boussard and Y. Mizumachi, "Production of Beams with High Line-Density by Azimuthal Combination of Bunches in a Synchrotron", CERN-SPS/ARF/79-11; 1979 IEEE Particle Accelerator Conference (1979).
- C. Ankenbrandt, "Slip-Stacking: A New Method of Momentum Stacking" Fermilab FN-352 (1981).
- <sup>6</sup> Reference to MARS10 program
- <sup>7</sup> CM Bhat and NV Mokhov, "Calculation of Beam Sweeping Effect for the Fermilab Antiproton Source", Fermilab-TM-1585 (1989)
- <sup>8</sup> FM Bieniosek, K Anderson and K Fullett, "Requirements for a Beam Sweeping System for the Fermilab Antiproton Source Target", Proc. of the 1995 US Particle Accelerator Conference, p1939. Dallas (1995); and FM Bieniosek, "A Beam Sweeping System for the Fermilab Antiproton Production Target", Fermilab-TM-1857 (1993)
- <sup>9</sup>G. Dugan et al.,IEEE Trans. Nucl. Sci.30:3660-3662(1983)
- <sup>10</sup>S.O'Day and K.Anderson, Proc. 1995 US Particle Accelerator Conference, Dallas, Texas
- <sup>11</sup> F. M. Bieniosek, pbar Note #550 (1994)
- [10] BF Bayanov, TA Vsevolozhskaya, GI Silvestrov, "Study of the Stresses in and Design Development of Cylindrical Lithium Lenses", Preprint 84-168, Institute of Nuclear Physics (Budker Institute), Novosibirsk (1985)
- <sup>12</sup>
- <sup>13</sup> [4] S O'Day, FM Bieniosek, "8.9 GeV Pbar Yield Measurements at the Fermilab Antiproton Source", Nuclear Instruments and Methods ,A343, p343 (1994)
- <sup>14</sup> Reference to MCLENS simulation
- <sup>15</sup>
- <sup>16</sup>S O'Day, FM Bieniosek, "Pbar Production Measurements at the Fermilab Antiproton Source", EPAC 94 Proceedings, p2438, London (1994)
- <sup>17</sup>Fermilab III Accelerator Upgrade Phase 1 (1990/94), unpublished.
- <sup>18</sup> D Olivieri, "A Dynamic Momentum Compaction Factor Lattice for Improvements to Stochastic Cooling in Storage Rings", Dissertation thesis for the University of Massachusetts, Amherst (1996)
- <sup>19</sup> Tevatron I Design Book
- <sup>20</sup> The van der Meer stack tail cooling model reference.
- <sup>21</sup> MEB E-Cool Design Report 1992, Indiana University Cyclotron Facility (October 1992)
- <sup>22</sup>National Electrostatics Corporation Newsletter, Fall 1990 (NEC, Graber Rd., Box 620310, Middleton, WI 53562 USA.
- <sup>23</sup> J.A. Ferry, et al., "Accelerator terminal voltage stability", NIM B64 (1992) 309-312.
- <sup>24</sup> T. Ellison, R. Brown, and B. DeVries, "The IUCF electron cooling system collector performance", NIM B40/41 (1989) 864-869.
- <sup>25</sup> S. Nagaitsev, et al., "The development of the technology for electron cooling in the 2-20 GeV/nucleon energy regime" in Proceedings of the 1993 Workshop on Beam Cooling, CERN Report No. 94-03, pp. 390-394.
- <sup>26</sup> Ioanis Kourbanis, talk given to the TeV33 working group, :Proton bunch formation iwht variable spacing," May 13, 1996 (unpublished).
- <sup>27</sup> Snowmass paper, evolution of stores.
- <sup>28</sup> Transverse head-tail instability
- <sup>29</sup> Longitudinal head-tail instability
- <sup>30</sup> 6x6 damper reference
- <sup>31</sup> C. Crawford, TM-1564.

---

<sup>32</sup> S.D. Holmes, et al., 132 nsec Bunch Spacing in the Tevatron Proton-Antiproton Collider, Fermilab Technical Memo #1920, Dec.23, 1994.